JAMES | Journal of Advances in Modeling Earth Systems®

RESEARCH ARTICLE
10.1029/2025MS005405

Key Points:

- We introduce an intermediate-complexity longwave radiative transfer scheme for climate models, the Simple Spectral Model (SSM)
- The SSM captures the spectral dependence of atmospheric absorption using analytic fits and is easy to understand and modify
- The SSM produces accurate climate states, and their response to warming, when implemented in a GCM, in stark contrast to gray schemes

Supporting Information:

Supporting Information may be found in the online version of this article.

Correspondence to:
A. I. L. Williams,
andrewwilliams@ucsd.edu

Citation:
Williams, A. I. L. (2026). Bridging clarity and accuracy: A simple spectral longwave radiation scheme for idealized climate modeling. *Journal of Advances in Modeling Earth Systems*, *18*, e2025MS005405. https://doi.org/10.1029/2025MS005405

Received 12 AUG 2025
Accepted 9 JAN 2026

Bridging Clarity and Accuracy: A Simple Spectral Longwave Radiation Scheme for Idealized Climate Modeling

Andrew I. L. Williams[1,2]

[1]Program in Atmospheric and Oceanic Sciences, Princeton University, Princeton, NJ, USA, [2]Scripps Institution of Oceanography, University of California San Diego, La Jolla, CA, USA

Abstract Parameterizing radiative transfer in climate models means navigating trade-offs between physical accuracy and conceptual clarity. However, currently available schemes sit at the extremes of this spectrum: correlated-k schemes are fast and accurate but rely on lookup tables which obscure the underlying physics and make such schemes difficult to modify, while gray radiation schemes are conceptually straightforward but introduce significant biases in atmospheric circulation. Here we introduce a Simple Spectral Model (SSM) for clear-sky longwave radiative transfer which bridges this "clarity-accuracy" gap. The SSM accomplishes this by representing the spectral structure of H_2O and CO_2 absorption using analytic fits at reference conditions, then uses simple functional forms to extend these fits to different atmospheric conditions. This, coupled to a simple, two-stream solver, yields a system of six equations and ten physically meaningful parameters which can solve for clear-sky longwave fluxes given atmospheric profiles of temperature and humidity. When implemented in an idealized aquaplanet GCM, the SSM produces zonal-mean climate states which accurately mimic the results using a benchmark correlated-k code. The SSM also alleviates the significant zonal-mean climate biases associated with using gray radiation, including an improved representation of radiative cooling profiles, tropopause structure, jet dynamics, and Hadley Cell characteristics both in control climates and in response to uniform warming. This work demonstrates that even a simple spectral representation of atmospheric absorption suffices to capture the essential physics of longwave radiative transfer. The SSM promises to be a valuable tool both for idealized climate modeling, and for teaching radiative transfer in the classroom.

Plain Language Summary The Earth is warmed by the sun, and cooled by emitting light out to space. This emission from the planet's surface is complicated by the existence of greenhouse gases, which absorb and re-emit the Earth's light. Representing these processes in climate models is important to successfully model the distribution of temperature and winds. Through decades of work we can now represent these processes to a high degree of accuracy, but the way we do this is difficult to understand unless you are an expert. Other methods exist which are easy to understand, but they do not give good representations of temperature or winds. In this paper I introduce a new method for representing the absorption and emission of light in the atmosphere. It is only a couple of equations and is easy to understand and to code up, but it is also very accurate and gives good representation of temperature and winds. This new approach is not meant to replace existing state-of-the-art methods, but rather to "fill in the gap" which exists between accurate methods which are hard-to-understand, and easy-to-understand methods which are inaccurate.

1. Introduction

Radiative transfer lies at the heart of Earth's climate system, governing the fundamental energy balance that drives atmospheric circulation and the hydrological cycle. Parameterizing radiation accurately and efficiently is therefore essential for developing useful general circulation models (GCMs). Line-by-line models exist which agree excellently with observations (Pincus et al., 2015) but these benchmark models are much too computationally expensive to be used in GCMs. This creates an inevitable "accuracy-efficiency" trade-off that must be navigated in climate model development.

Beyond computational considerations, another critical factor must be balanced when developing radiative transfer schemes: their clarity and intelligibility. This axis of consideration follows from Isaac Held's influential 2005 essay where he cautioned against the growing "gap between simulation and understanding" in climate modeling (Held, 2005). Even if parameterization schemes are accurate, a lack of clarity hampers our ability to design creative experiments and test hypotheses (Jeevanjee et al., 2017; Reed et al., 2025). It is this trade-off between

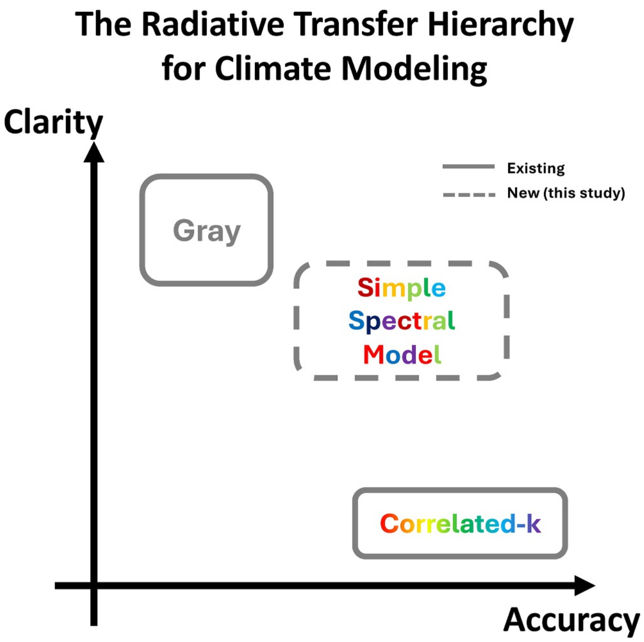

Figure 1. A planar hierarchy of radiative transfer approaches for climate modeling. The different classes of radiative transfer schemes are grouped by their "clarity" (vertical axis) and their "accuracy" (horizontal axis). Both terms are used loosely, in a way which is defined in the main text. The Simple Spectral Model and correlated-k schemes are written using a rainbow font to highlight that they are *spectral* representations of radiative transfer, as opposed to the gray schemes, which do not explicitly represent the spectral nature of light.

clarity and accuracy that we will focus on in this paper, with an eye toward developing a simple radiative transfer scheme which balances these two constraints.

The current state of affairs, focusing on the representation of gas absorption, is sketched in Figure 1, which groups different classes of radiative transfer schemes according to their "clarity" and "accuracy." Modern climate models typically parameterize gas absorption using correlated-k methods, such as RRTMG (Iacono et al., 2008; Mlawer et al., 1997) and its successor RTE + RRTMGP (Pincus et al., 2019). These schemes typically split the electromagnetic spectrum into bands and use precomputed lookup tables to represent the spectral variation of gaseous absorption in a computationally efficient way. Correlated-k schemes can achieve high accuracy when applied within their calibration range (Pincus et al., 2015), and thus score highly on the "accuracy" axis.

However, this accuracy often comes at the cost of clarity. The extensive use of lookup tables can obscure the underlying physics and means that modifying these schemes typically requires specialist knowledge, limiting their accessibility for hypothesis-driven experimentation or educational purposes (Hogan & Matricardi, 2020). Furthermore, correlated-k schemes often provide only broadband output or spectral output aggregated into coarse bands, limiting the ability to link model output to spectrally resolved radiative processes. Hence, while correlated-k schemes represent the state-of-the-art for radiative transfer in GCMs, their complexity can pose challenges for interpretability and pedagogical use.

Sitting at the opposite end of the "clarity-accuracy" spectrum we have "gray" radiation schemes. Gray radiation schemes neglect the spectral dependence of atmospheric absorption and emission, and in practice often directly prescribe analytic profiles of optical depth as a function of pressure. This greatly simplifies the mathematics of radiative transfer, offering conceptual clarity, analytical tractability, and the ability to easily modify the scheme to test hypotheses (e.g., Lutsko & Popp, 2018). This high score on the "clarity" axis (Figure 1) has spurred the wide adoption of gray radiation schemes (most notably the Frierson et al. (2006) scheme) in idealized GCM studies, yielding insights into the hydrological cycle (S. M. Kang et al., 2008; O'Gorman & Schneider, 2008; Schneider et al., 2010), atmospheric dynamics (Davis & Birner, 2022; Lewis et al., 2024; Wills et al., 2017), and exoplanets (Guendelman & Kaspi, 2020; Kaspi & Showman, 2015; Merlis & Schneider, 2010). However, it is well-known that gray schemes do not accurately represent the structure of radiative heating in the atmosphere (e.g., Jeevanjee & Fueglistaler, 2020b) and there is increasing realization in the community that gray radiation distorts many aspects of the atmospheric circulation and its response to warming (Davis & Birner, 2022; Tan et al., 2019). Hence, although gray schemes are conceptually simple and easy-to-use, they score poorly on the "accuracy" scale in Figure 1.

As Figure 1 illustrates, there is a conspicuous gap in the middle ground—we lack a radiation scheme that combines reasonable accuracy with reasonable clarity. Recent advances in "simple spectral models" (SSMs) offer an opportunity to fill this gap. Work by Koll and Cronin (2018), Jeevanjee and Fueglistaler (2020b), Romps et al. (2022), and Cohen and Pincus (2025), among others, has shown that simplified representations of H_2O and CO_2 spectroscopy can capture the essential physics while remaining analytically tractable. This "pencil-and-paper" approach has yielded valuable insights into radiative forcing and feedbacks, hydrological sensitivity, and the vertical structure of radiative cooling. However, despite their theoretical utility, simplified spectroscopic models of radiative transfer have not yet been implemented in GCMs.

Here, we address the "clarity-accuracy" gap in Figure 1 by developing a simple spectral model (SSM) for clear-sky, longwave radiative transfer in a GCM. The SSM combines the two-stream equations with analytical approximations to absorption coefficients, providing the spectral detail required for accurate radiative transfer while retaining analytical simplicity. When implemented in an idealized aquaplanet GCM, the SSM greatly reduces biases present when using a representative gray scheme (Frierson et al., 2006).

We focus on the longwave as it is the dominant source of radiative heating in Earth-like atmospheres, and as previous work on SSMs has focused mostly on the longwave. However, we view the current work only as a first step toward filling the "clarity-accuracy" gap in Figure 1, and as a complement to more advanced schemes like RTE + RRTMGP that prioritize accuracy and flexibility through different means.

We proceed as follows: In the next section, we will document the Simple Spectral Model (SSM) in terms of its governing equations and analytic approximations. Then we implement a hierarchy of longwave radiative transfer schemes (gray, SSM, RRTMG) in an idealized aquaplanet GCM and describe the resulting control climates and their response to uniform warming. We then use a single-column model to explore state-dependence of the longwave radiative feedback parameter in the SSM, with a focus on extremely warm climate states. The conclusion discusses paths forward for and applications of the SSM.

2. Constructing the Simple Spectral Model

2.1. Overview

In this section we will construct a simple spectral model (SSM) for clear-sky, longwave radiative transfer. Our SSM computes upward and downward longwave fluxes using the standard Schwarzschild's equations for flux in the presence of emission and absorption:

$$\frac{dF^{\uparrow}_{\tilde{\nu}}}{d\tau_{\tilde{\nu}}} = F^{\uparrow}_{\tilde{\nu}} - \pi B_{\tilde{\nu}}(T) \tag{1}$$

$$\frac{dF^{\downarrow}_{\tilde{\nu}}}{d\tau_{\tilde{\nu}}} = \pi B_{\tilde{\nu}}(T) - F^{\downarrow}_{\tilde{\nu}} \tag{2}$$

where T is the temperature, and $\tau_{\tilde{\nu}}$ and $B_{\tilde{\nu}}(T)$ are the longwave optical depth and Planck function at wavenumber $\tilde{\nu}$, respectively. The boundary condition at the top of the atmosphere is $F^{\downarrow}_{\tilde{\nu},\mathrm{TOA}} = 0$, and the boundary condition at the surface is $F^{\uparrow}_{\tilde{\nu},\mathrm{sfc}} = \pi B_{\tilde{\nu}}(T_{\mathrm{sfc}})$. We assume a unit surface emissivity, but this could easily be adjusted.

In addition to the boundary conditions, to solve Equations 1 and 2 we also need to know the optical depth, $\tau_{\tilde{\nu}}(p)$. We calculate this as

$$\tau_{\tilde{\nu}}(p) = D\int_0^p \kappa(\tilde{\nu}, T, p)\, q_{\mathrm{GHG}} \frac{dp'}{g} \tag{3}$$

where $D = 1.5$ is a diffusivity factor required by the two-stream approximation (Armstrong, 1968; Clough et al., 1992; Pierrehumbert, 2010). κ is the mass absorption coefficient, which depends not only on wavenumber $\tilde{\nu}$ but also on T and p, due to temperature scaling and pressure broadening. q_{GHG} is the mass-specific concentration (units of kg kg^{-1}) of the longwave absorber, which for H_2O is the specific humidity, q_v. For well-mixed (dilute) CO_2, q_{CO_2} is the ppmv of CO_2 multiplied by the ratio of the molar masses of CO_2 and dry air; for example for 280 ppmv of CO_2, $q_{CO_2} = 280 \times 10^{-6} \times (44/29)$.

2.2. Analytically Approximating the Absorption Coefficients

To calculate the spectrally resolved optical depth, $\tau_{\tilde{\nu}}$ we need to know the mass absorption coefficient, $\kappa_{\tilde{\nu}}$, but what does this look like? In Figure 2, we plot the mass absorption coefficients for H_2O line absorption (in blue), continuum absorption (in pink) and CO_2 line absorption (in orange) as a function of wavenumber. Line data are taken from the HITRAN2016 spectroscopic database (Gordon et al., 2017) and the H_2O continuum is represented using the MT_CKD_3.2 model (Mlawer et al., 2012). The absorption coefficients are calculated at a reference pressure of 500 hPa, a temperature of 260 K, and 100% relative humidity using the PyRADS model (Koll & Cronin, 2018). The data are sampled at a spectral resolution of 0.01 cm^{-1}, and line data plotted as partially transparent dots such that darker colors correspond to a higher density of absorbing wavenumbers.

The complexity of the spectral features in Figure 2 is striking; the absorption spectrum is made up of innumerable absorption lines, each with their own strength, with line strengths varying by many orders of magnitude across the

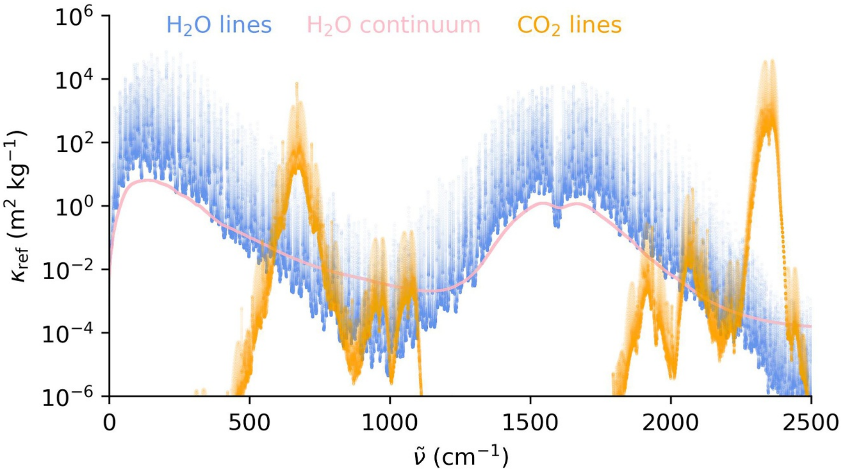

Figure 2. Reference mass absorption coefficients ($\mathrm{m^2\ kg^{-1}}$) for H_2O line absorption (light blue), continuum absorption (light pink) and CO_2 line absorption (orange) at $\left(T_{\mathrm{ref}}, p_{\mathrm{ref}}\right)$ = (260 K, 500 hPa) and 100% relative humidity calculated using PyRADS (Koll & Cronin, 2018).

longwave spectrum. However, despite this fine-scale complexity, there is large-scale "structure" to the absorption coefficients. For example, H_2O line absorption exhibits multiple well-known "bands," such as the pure rotation band ($200 < \tilde{\nu} < 1000\ \mathrm{cm^{-1}}$), the vibration-rotation band ($1000 < \tilde{\nu} < 1450\ \mathrm{cm^{-1}}$), and the combination band ($1700 < \tilde{\nu} < 2500\ \mathrm{cm^{-1}}$). In these bands, line absorption either declines exponentially with wavenumber (rotation, combination), or increases exponentially (vibration-rotation). Also notable are the H_2O "window" regions, where line absorption is very weak and where continuum absorption dominates over line absorption. The most notable of these is the window region centered around 1000 $\mathrm{cm^{-1}}$. CO_2 also has a complicated spectral structure, organized into a series of exponential increases and decays which appear as "triangles" on the logarithmic axis used in Figure 2. Of particular interest for Earth-like climates is the prominent absorption feature around 667 $\mathrm{cm^{-1}}$ (sometimes referred to as the "15 µm band"), which is close to the peak of the Planck radiation curve for an Earth-like blackbody (Wordsworth et al., 2024). CO_2 also has opacity in other bands, but the "15 µm band" is the source of the vast majority of radiative forcing at modern atmospheric concentrations (Mlynczak et al., 2016; Romps et al., 2022).

Efficiently representing this spectral structure is a key problem in parameterizing radiative transfer for GCMs. Correlated-k models typically achieve this by splitting the spectrum into a small number of bands, performing a number of "pseudo-monochromatic" calculations within these bands. In practice, lookup tables are generated for a number of different temperatures and pressures and the results are linearly interpolated to the GCM temperature and pressure at runtime. On the other hand, gray models neglect this spectral structure entirely and instead use absorption coefficients (or more commonly, optical depths) which are independent of wavenumber (Frierson et al., 2006; Jeevanjee & Fueglistaler, 2020b). These differences neatly reflect the "clarity-accuracy" trade-off made by these two approaches (Figure 1): correlated-k methods are more accurate but rely heavily on empirical representations of the underlying spectroscopy, whereas gray schemes represent the spectroscopy simply, but inaccurately.

In contrast to these two approaches, the key principle of simple spectral modeling is that we can neglect the fine-scale spectroscopic details of $\kappa_{\tilde{\nu}}$ and instead represent its "large-scale" spectral variations using analytical fits. It is not obvious a priori that this should work, but we will show that solely representing the "large-scale" structure of $\kappa_{\tilde{\nu}}$ is sufficient to capture many key features necessary for an accurate climate simulation. Using analytical fits to represent $\kappa_{\tilde{\nu}}$ in a GCM's radiative transfer scheme builds off of previous work (e.g., Cohen & Pincus, 2025; Jeevanjee & Fueglistaler, 2020b; Koll et al., 2023; Spaulding-Astudillo & Mitchell, 2025; Wilson & Gea-Banacloche, 2012) which have used similar approximations to develop pencil-and-paper models of radiative cooling and climate feedbacks, and early work by Crisp et al. (1986) who used an analytic approximation to CO_2's absorption spectrum when developing an early radiative transfer parameterization.

We begin by outlining the analytical fits we use to parameterize line absorption from H_2O and CO_2, and continuum absorption from H_2O. We perform these fits at the reference conditions outlined above, then use simple scalings to extend the results to different temperatures and pressures.

For line absorption from H_2O, we approximate the reference absorption coefficients as a piecewise function of wavenumber, $\tilde{\nu}$,

$$\kappa^{\mathrm{ref}}_{\mathrm{H_2O,line}} = \begin{cases} \kappa_{\mathrm{rot}} & \text{if } \tilde{\nu} \in \left[10\,\mathrm{cm}^{-1}, 200\,\mathrm{cm}^{-1}\right] \\ \kappa_{\mathrm{rot}} \exp\left(-\dfrac{\tilde{\nu} - 200}{l_{\mathrm{rot}}}\right) & \text{if } \tilde{\nu} \in \left[200\,\mathrm{cm}^{-1}, 1000\,\mathrm{cm}^{-1}\right] \\ \kappa_{\mathrm{vr}} \exp\left(-\dfrac{1450 - \tilde{\nu}}{l_{\mathrm{vr},1}}\right) & \text{if } \tilde{\nu} \in \left[1000\,\mathrm{cm}^{-1}, 1450\,\mathrm{cm}^{-1}\right] \\ \kappa_{\mathrm{vr}} & \text{if } \tilde{\nu} \in \left[1450\,\mathrm{cm}^{-1}, 1700\,\mathrm{cm}^{-1}\right] \\ \kappa_{\mathrm{vr}} \exp\left(-\dfrac{\tilde{\nu} - 1700}{l_{\mathrm{vr},2}}\right) & \text{if } \tilde{\nu} \in \left[1700\,\mathrm{cm}^{-1}, 2500\,\mathrm{cm}^{-1}\right] \end{cases} \tag{4}$$

where the "rot" and "vr" subscripts are shorthand for the "rotation" and "vibration–rotation" bands of H_2O.

For CO_2, we approximate the reference absorption coefficients as

$$\kappa^{\mathrm{ref}}_{\mathrm{CO_2}} = \kappa_{\mathrm{CO_2}} \exp\left(-\frac{|\tilde{\nu} - \tilde{\nu}_{\mathrm{CO_2}}|}{l_{\mathrm{CO_2}}}\right) \quad \text{if } \tilde{\nu} \in \left[500\,\mathrm{cm}^{-1}, 850\,\mathrm{cm}^{-1}\right]. \tag{5}$$

This formulation (Equation 5) focuses on the strongly absorbing "bending mode" of CO_2 and ignores the absorption from secondary CO_2 bands. We find this to be a reasonable approximation, but other modes of CO_2 absorption could easily be added back into the SSM by defining a piece-wise $\kappa^{\mathrm{ref}}_{\mathrm{CO_2}}$ as we have done for H_2O.

H_2O continuum absorption is of primary importance in the atmospheric window regions, so we model H_2O continuum absorption as two separate, gray, absorbers:

$$\kappa^{\mathrm{ref}}_{\mathrm{H_2O,cnt}} = \begin{cases} \kappa_{\mathrm{cnt},1} & \text{if } \tilde{\nu} \in \left[10\,\mathrm{cm}^{-1},\ 1700\,\mathrm{cm}^{-1}\right] \\ \kappa_{\mathrm{cnt},2} & \text{if } \tilde{\nu} \in \left[1700\,\mathrm{cm}^{-1},\ 2500\,\mathrm{cm}^{-1}\right]. \end{cases} \tag{6}$$

In total, our model of H_2O and CO_2 spectroscopy has 10 parameters (Table 1). To fit these parameters, we first group the absorption coefficients into 25 cm^{-1} bins and calculate the median absorption coefficient in each bin. We take the median because the average transmission across a spectral band tends to be dominated by the most optically thin frequencies (Koll et al., 2023; Pierrehumbert, 2010). We then use scipy.optimize.curve_fit to fit Equations 4–6 to these coarse-grained absorption coefficients (Virtanen et al., 2020). We first fit Equation 4 to the line absorption for H_2O only, then use these parameters to fit our continuum model (Equation 6) to the sum of line and continuum absorption. We fit Equation 5 to the line absorption for CO_2 in isolation. The results of this fitting procedure are shown in Table 1. The results are somewhat sensitive to the details of the fitting procedure, but not to the extent that they qualitatively affect the accuracy of the resultant GCM simulation.

Figure 3 shows the reference absorption coefficients for CO_2 (in the region of the 15 μm band) and H_2O (the sum of line and continuum absorption) for the PyRADS line-by-line model, the coarse-grained absorption coefficients, and the piece-wise analytic fits from Equations 4–6. Overall, the piece-wise approximations capture the shape of the absorption coefficients fairly well. There is a slight underestimation of H_2O absorption at the edge of the main window region, but this is a region where absorption from CO_2 dominates and so we still consider the fits in Figure 3 to be adequate.

To extend these fitted absorption coefficients beyond reference conditions we multiply $\kappa^{\mathrm{ref}}_{\mathrm{CO_2}}$ and $\kappa^{\mathrm{ref}}_{\mathrm{H_2O,line}}$ by a pressure-scaling factor, p/p_{ref}, which accounts for "foreign-broadening" of spectral lines due to collisions with other molecules (Pierrehumbert, 2010). To keep the model simple we neglect any temperature-scaling of the reference absorption coefficients for line absorption (as in Jeevanjee & Fueglistaler, 2020b; Koll et al., 2023; Cohen & Pincus, 2025). The H_2O continuum experiences "self-broadening" and thus scales with the water vapor pressure, $p_v/p_{v,\mathrm{ref}}$ (Jeevanjee, Seeley, et al., 2021; Shine et al., 2012). We also include an exponential temperature-dependence of the continuum, $e^{\sigma(T_{\mathrm{ref}}-T)}$, following Mlawer et al. (1997), with $\sigma = 0.02\ \mathrm{K}^{-1}$.

Including these pressure- and temperature-scalings, our analytical representations of H_2O line absorption, H_2O continuum absorption & CO_2 line absorption are:

$$\kappa_{\mathrm{H_2O,line}}(\tilde{\nu},p) = \left(\frac{p}{p_{\mathrm{ref}}}\right)\kappa^{\mathrm{ref}}_{\mathrm{H_2O,line}}(\tilde{\nu}), \tag{7}$$

$$\kappa_{\mathrm{H_2O,cnt}}(\tilde{\nu},p,T) = \left(\frac{p_v}{p_{v,\mathrm{ref}}}\right)e^{\sigma(T_{\mathrm{ref}}-T)}\,\kappa^{\mathrm{ref}}_{\mathrm{H_2O,cnt}}(\tilde{\nu}), \tag{8}$$

and,

$$\kappa_{\mathrm{CO_2}}(\tilde{\nu},p) = \left(\frac{p}{p_{\mathrm{ref}}}\right)\kappa^{\mathrm{ref}}_{\mathrm{CO_2}}(\tilde{\nu}). \tag{9}$$

Table 1
Spectroscopic Parameters in the Simple Spectral Model (SSM)

Parameter	Value	Unit
κ_{rot}	37	$\mathrm{m}^2\ \mathrm{kg}^{-1}$
κ_{vr}	5	$\mathrm{m}^2\ \mathrm{kg}^{-1}$
l_{rot}	56	cm^{-1}
$l_{\mathrm{vr},1}$	37	cm^{-1}
$l_{\mathrm{vr},2}$	52	cm^{-1}
$\kappa_{\mathrm{cnt},1}$	0.004	$\mathrm{m}^2\ \mathrm{kg}^{-1}$
$\kappa_{\mathrm{cnt},2}$	0.0002	$\mathrm{m}^2\ \mathrm{kg}^{-1}$
$\kappa_{\mathrm{CO_2}}$	110	$\mathrm{m}^2\ \mathrm{kg}^{-1}$
$\tilde{\nu}_{\mathrm{CO_2}}$	667	cm^{-1}
$l_{\mathrm{CO_2}}$	12	cm^{-1}

Note. These are the reference values, taken at $(T_{\mathrm{ref}},\ p_{\mathrm{ref}},\ \mathrm{RH}_{\mathrm{ref}}) = (260\ \mathrm{K}, 500\ \mathrm{hPa}, 100\%)$.

We have now constructed our SSM. With Equations 1–3 and 7–9 in hand, and the parameters in Table 1, we can simulate longwave fluxes upwards and downwards through the atmosphere given profiles of temperature and humidity. We note that our SSM differs from that of Jeevanjee and Fueglistaler (2020b) in that they invoke the "cooling-to-space" approximation, whereas we numerically integrate the radiative transfer equations (Equations 1–3).

As a sanity check, in Appendix A we implement our SSM in a single-column model and show it can reproduce the state-dependence of the longwave feedback parameter found by previous studies (Koll et al., 2023; Stevens & Kluft, 2023). We note that the SSM's detailed spectral output also allows us to easily understand the radiative processes involved, in contrast to broadband radiation schemes. Satisfied that our SSM can reproduce previous single-column model results, next we implement our SSM scheme in an idealized GCM and compare the resulting zonal-mean climate to that obtained with a gray scheme and RRTMG.

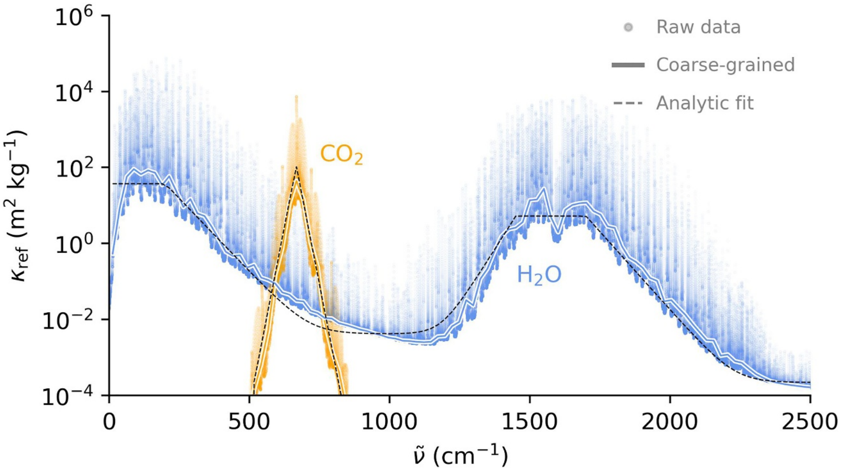

Figure 3. Reference mass absorption coefficients ($\mathrm{m}^2\ \mathrm{kg}^{-1}$) for H_2O line and continuum absorption (light blue) and CO_2 line absorption (orange) at $(T_{\mathrm{ref}},\ p_{\mathrm{ref}}) = (260\ \mathrm{K},\ 500\ \mathrm{hPa})$ and 100% relative humidity calculated using PyRADS (Koll & Cronin, 2018). We only consider CO_2 absorption in the 500–850 cm^{-1} range, but this could easily be extended if the user desires. The coarse-grained absorption coefficients for CO_2 and H_2O are shown in the thick lines, and the dashed black lines show the piece-wise analytic fits to these coarse-grained absorption coefficients.

3. Idealized GCM Simulations

3.1. Model Setup

The idealized aquaplanet GCM we use is a configuration of Isca (Vallis et al., 2018) that follows closely Frierson et al. (2006) and O'Gorman and Schneider (2008). The representation of physical processes in the atmosphere is idealized in a variety of ways: the "microphysics" is a saturation adjustment to 100% relative humidity using an idealized formulation of the Clausius–Clapeyron relation, condensed water instantaneously falls to the surface as precipitation, a simplified Betts-Miller scheme relaxes convectively unstable profiles toward a moist adiabat with a 2-hr timescale (Frierson, 2007), and there is no representation of sea-ice in the model. The model also has no representation of clouds, which is appropriate as our focus is on the climatic impacts of differences in clear-sky radiative transfer.

We force the model using the Earth-like "QOBS" sea-surface temperature (SST) distribution from Neale and Hoskins (2000), and to evaluate the modeled response to climate change we also run simulations where the SSTs are uniformly warmed by 4 K. In Appendix B we show that our conclusions are unchanged if we examine slab ocean simulations with an increased solar constant instead of using fixed-SST experiments.

All simulations are performed at T42 spectral truncation ($\approx 2.8^\circ$ horizontal resolution) with 50 vertical levels in the model's sigma (pressure divided by surface pressure) coordinate and are integrated for 6,000 days. The analysis is conducted over the final 3,000 days once the simulations have reached a steady-state. Because of the symmetries of the boundary conditions the simulated climates are zonally and hemispherically symmetric, we thus average all fields zonally and between the hemispheres.

We run the model with a hierarchy of clear-sky longwave radiative transfer schemes. Specifically, we run Isca with our longwave simple spectral model (SSM) and compare the results to simulations using either gray radiation or a correlated-k scheme. As a representative gray scheme we use the Frierson et al. (2006) scheme. The correlated-k scheme we use is RRTMG (Iacono et al., 2008; Mlawer et al., 1997). We do not include cloud radiative effects or ozone in any of our simulations, and run the SSM and RRTMG with 300ppmv of CO_2.

The Frierson et al. (2006) scheme computes longwave fluxes using the spectrally integrated versions of Equations 1 and 2, and a gray optical depth which is a prescribed function of latitude and pressure,

$$\tau_{\mathrm{lw}}(p,\phi) = \left[f\sigma + (1-f)\sigma^4\right]\left[\tau_e + (\tau_p - \tau_e)\sin^2(\phi)\right], \tag{10}$$

where $\sigma = p/p_s$. Frierson et al. (2006) take $\tau_e = 6$, $\tau_p = 1.5$, and $f = 0.1$ as their parameter values, but this parameter set is not unique and previous studies have used different values for (τ_e, τ_p, f). However, because the Frierson et al. (2006) scheme is the most commonly used gray radiation scheme, we focus on their parameter set in the main text. Our conclusions are unchanged if we instead use other parameter values in the literature (see Appendix C).

To aid comparison between the hierarchy of different longwave radiation schemes, we disable atmospheric absorption of shortwave radiation. Hence any differences in the climates of our fixed-SST simulations come purely from the representation of longwave radiative transfer.

At each GCM timestep, we solve the SSM equations at 100 equally spaced wavenumbers between 10 cm^{-1} and 2500 cm^{-1}, then spectrally integrate to get the broadband heating rates. The reason for running at this relatively high spectral resolution is to make it easier to examine spectral features of the output, but the GCM results are qualitatively similar if we solve the equations either at 20 equally spaced wavenumber points, or extend the upper-bound of wavenumber space to 3000 cm^{-1}.

The focus of this paper is not on the "efficiency-accuracy" trade-off, which has been discussed in detail by other authors (e.g., Pincus et al., 2019), but we note in passing that running the GCM with our SSM using 100 wavenumber points is about twice as fast as running the GCM with RRTMG_LW.

3.2. Control Climate

In Figure 4 we compare the time-averaged, zonal-mean climates of the idealized GCM coupled to the three longwave radiation schemes. Because the GCM simulations are run with Earth-like SSTs and thus are within

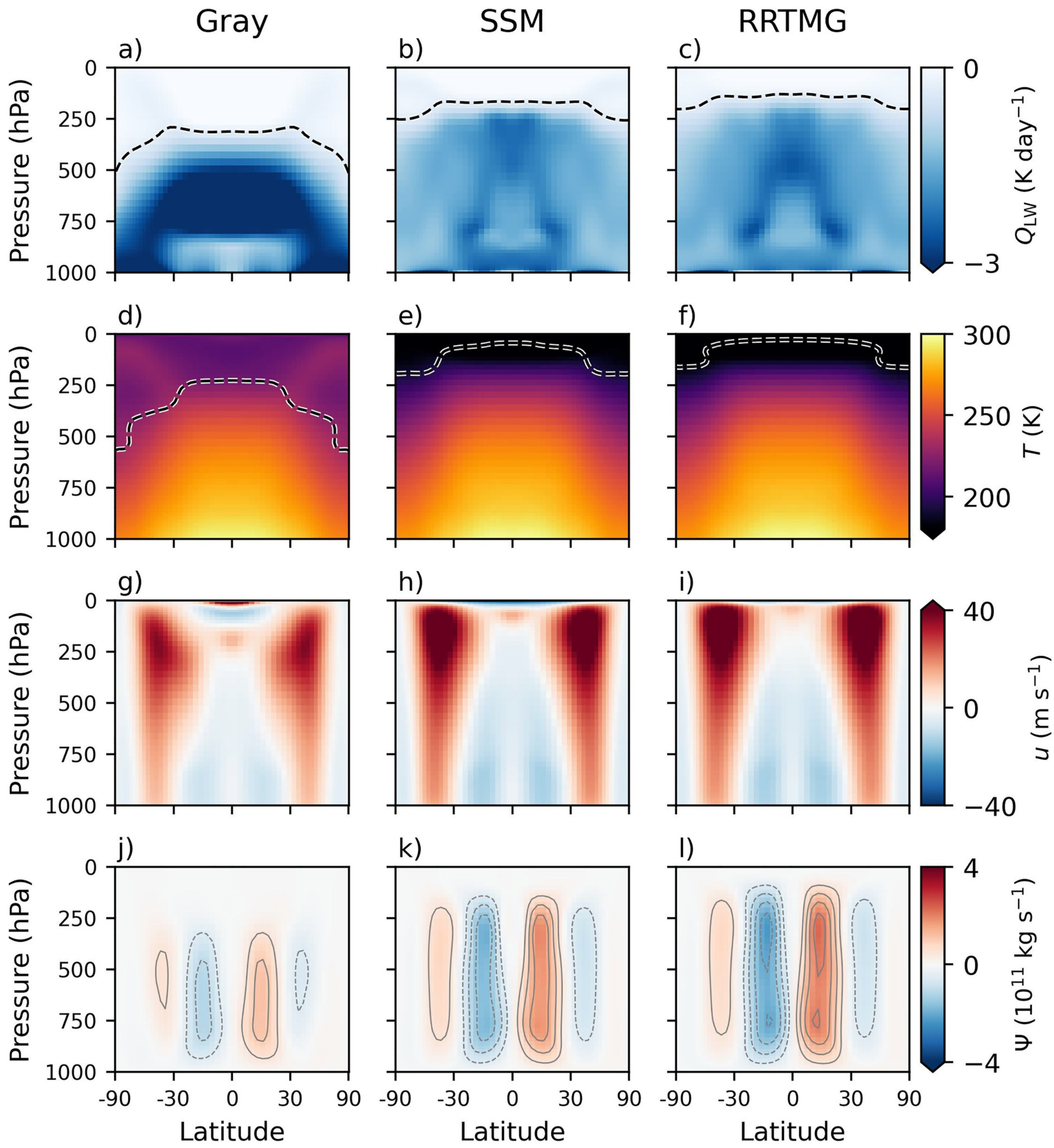

Figure 4. Zonal-mean (a–c) longwave radiative heating rate, (d–f) temperature, (g–i) zonal wind, and (j–l) mean meridional streamfunction for GCM simulations using (left column) gray radiation, (middle column) the simple spectral model, and (right column) RRTMG_LW. Contours in (a–c) and (d–f) are the radiative and lapse-rate tropopause respectively, diagnosed as the -0.3 K day^{-1} and -5 K km^{-1} contours (McKim et al., 2025). Contours in (j–l) are plotted at $5x10^{10}$ kg s^{-1} intervals, with negative contours dashed and the zero contour omitted. Horizontal axis is the sine of latitude.

RRTMG's range of validity, we will treat the RRTMG results as a benchmark against which to compare the results using gray scheme and the SSM.

The longwave heating rate is negative throughout the troposphere, indicating that the atmosphere is cooled by longwave emission (Figures 4a–4c). However, while RRTMG and SSM generate a radiative cooling profile which is around ≈ -2K day^{-1} throughout the troposphere (Jeevanjee & Fueglistaler, 2020b), the gray model produces a pronounced "bulge" of radiative cooling in the upper troposphere whose magnitude is much larger (peaking at around -5 K day^{-1}). These differences in the radiative cooling profiles can be understood simply through the "unit optical depth" approximation, which states that the radiative cooling (specifically the cooling-to-space), maximizes at the level where $\tau = 1$ (e.g., Jeevanjee & Fueglistaler, 2020a; Petty, 2006). For gray schemes, the optical depth has no wavenumber-dependence, and so there is a single "$\tau = 1$" level where all of the radiative cooling becomes concentrated, whereas for the SSM and RRTM there are a range of "$\tau = 1$" levels throughout the atmosphere (each at a different wavenumber), yielding a more diffuse radiative cooling profile. There are small differences between the SSM and RRTMG configurations (differences between SSM and RRTMG are shown in Figure S1 in Supporting Information S1), but the SSM nevertheless produces a significantly more accurate simulation of longwave cooling profiles—that is, closer to RRTMG—compared to the gray model.

The pressure at which the radiative cooling approaches zero denotes the "radiative tropopause," which separates the dynamically active troposphere (where radiative cooling is balanced by heating from convection and eddies) from the largely quiescent stratosphere (which is approximately in radiative equilibrium). The radiative tropopause, diagnosed as the upper-tropospheric -0.3 K day^{-1} contour, is significantly lower in the atmosphere in the gray model compared to the SSM or RRTMG configurations, and also has a more pronounced latitudinal structure (Figures 4a–4c).

The most notable differences in zonal-mean temperature between the gray scheme and the SSM/RRTMG schemes are in the upper-troposphere and stratosphere (Figures 4d–4f). For example, the lapse-rate tropopause, diagnosed at the level where the lapse-rate first falls below -5 K km $^{-1}$ following McKim et al. (2025), is lower down in the atmosphere in the gray configuration compared to RRTMG or indeed the SSM. This is consistent with the radiative tropopause. SSM exhibits a small "too-low" bias in both the lapse-rate and radiative tropopause (Figure S1 in Supporting Information S1). The tropically averaged radiative tropopause pressure, defined as the area-weighted radiative tropopause pressure between ±30°N, is 313 hPa for gray, 184 hPa for SSM, and 136 hPa for RRTMG), which is consistent with previous work by McKim et al. (2025) who showed that the temperature (and height) of the tropopause is tied to water vapor's maximum absorption coefficient, which is underestimated by our piece-wise analytic fits (Figure 3).

We also note that the stratospheric temperature is much warmer in the gray configuration compared to RRTMG or SSM. As noted by Pierrehumbert (2010), for real gases the stratospheric temperature is not constrained by the planet's skin temperature and thus real gases can have much colder stratospheres than gray gases. The SSM's stratospheric temperature is similar to RRTMG's but has a noticeable "too warm" bias, particularly in the tropics (Figure S1 in Supporting Information S1). A notable feature of the gray model, not present in SSM or RRTMG, is temperature inversions in the extratropical stratosphere at around 200 hPa, where temperatures again increase with height. Such temperature inversions are a ubiquitous, but poorly understood, aspect of gray radiation aquaplanet simulations (e.g., Levine & Schneider, 2011; Schneider & O'Gorman, 2008; Singh & O'Gorman, 2012; Tan et al., 2019), and result in a reversed meridional temperature gradient in the stratosphere of the gray model, where tropical temperatures are colder than extratropical/polar temperatures. Many of these features of the gray model were previously noted by Tan et al. (2019).

Because of thermal wind balance, the different temperature structures in the three models result in different zonal wind profiles (Figures 4g–4i). All three configurations produce a deep, eddy-driven jet which drives surface westerlies but the gray model produces a shallower and weaker jet compared to the models with RRTMG or SSM. The latitude of the eddy-driven jet, diagnosed as the latitude of maximum 850 hPa zonal-mean zonal wind (S. M. Kang & Polvani, 2011), is about 41–42° for all three configurations. However, the subtropical jet latitude, diagnosed as the latitude of maximum zonal-mean zonal wind between 50 and 400 hPa with the 850 hPa wind removed (Waugh et al., 2018), is 26° for the gray model compared to 34° for the SSM and 36° for RRTMG. This "split jet" in the gray model is consistent with the fact that the tropopause "break," the region of maximum baroclinicity where the tropopause abruptly shifts from its tropical to extratropical altitude, is about 10° further equatorward in the gray model compared to either the RRTMG or SSM configurations. The subtropical jet is also weaker in the gray model compared to RRTMG, consistent with the idea that the thermal wind relation is integrated over a shallower troposphere in the gray model (Tan et al., 2019). We note that all schemes exhibit equatorial superrotation in the upper-troposphere, which is a common feature of equinoctial aquaplanet simulations (e.g., Zurita-Gotor & Held, 2024, 2025).

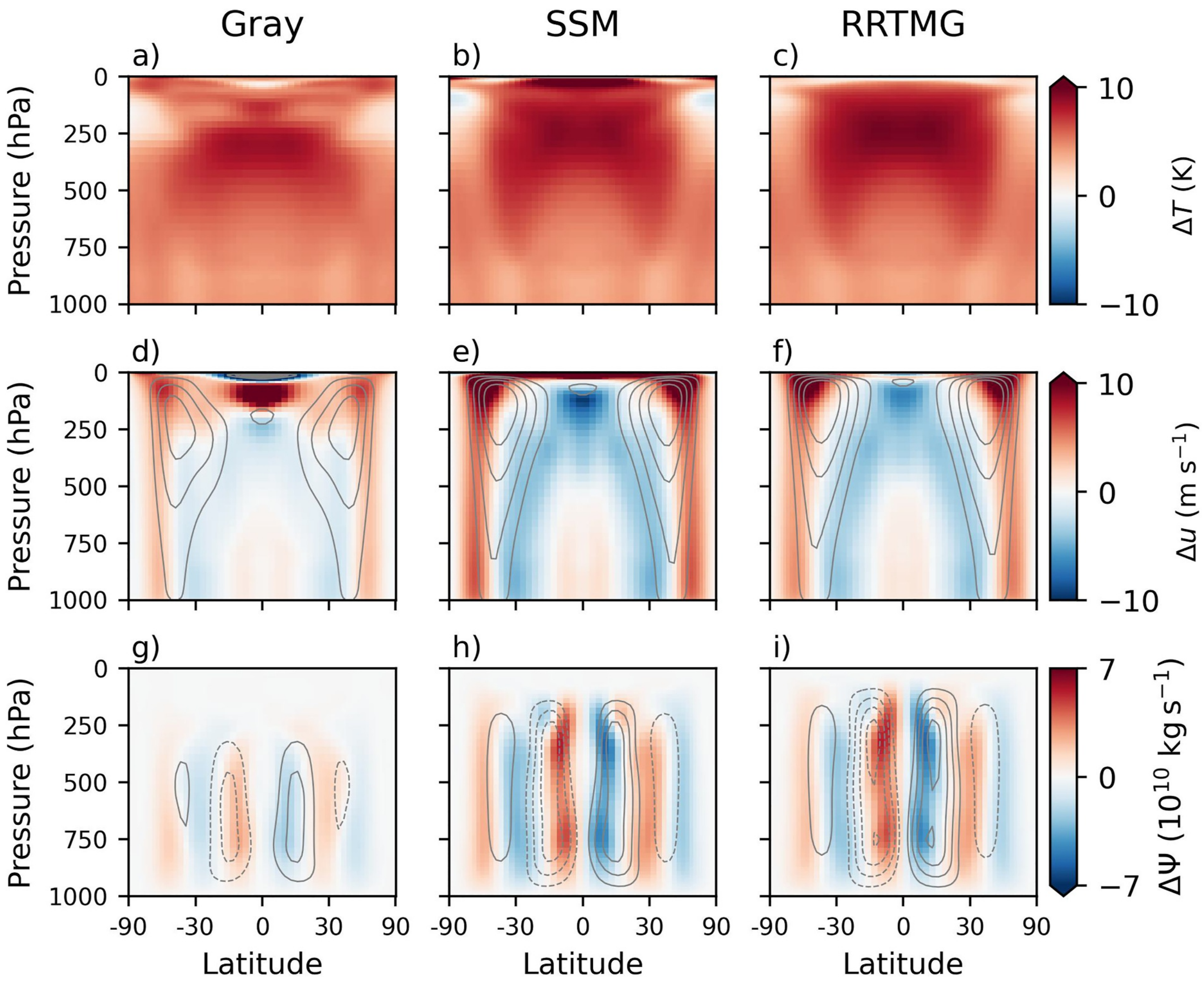

Figure 5. Zonal-mean changes in (a–c) temperature, (d–f) zonal wind, and (g–i) mean meridional streamfunction in response to uniform warming for the GCM with gray radiation (left column), the SSM (middle column), and RRTMG_LW (right column). Contours in (d–f) represent the 10, 20, 30, 40 m s^{-1} winds in the control run. Contours in (g–i) are the same as (j–l) of Figure 4. Horizontal axis is the sine of latitude.

In Figures 4j–4l we show the mean meridional streamfunction, calculated as

$$\psi(p,\phi) = \frac{2\pi a\cos(\phi)}{g}\int_p^0 [v]dp, \tag{11}$$

where p is the pressure, ϕ is the latitude, $a = 6,371$ km is the mean radius of Earth, $g = 9.81$ m s^{-1} is the acceleration due to gravity, v is the meridional wind, and square brackets indicate the zonal-mean. All three radiation schemes produce Hadley cells of similar latitudinal width. However, the gray scheme exhibits a weaker and shallower Hadley cell compared to the SSM and RRTMG, consistent with its more equatorward jet structure and lower tropopause height.

3.3. Response to Uniform Warming

The SSM's idealized representation of spectroscopy also captures key features of the coupling between radiation and dynamics under warming, as shown by Figure 5 where we plot the change in zonal-mean temperature (a–c), zonal wind (d–f), and mean meridional streamfunction (g-i) in response to a uniform 4 K warming of the SSTs. The SSM also accurately simulates the response to forcing in slab ocean simulations (Appendix B), but for simplicity we focus on the uniform warming case here.

Table 2

Summary of Climate Metrics Assessed in the Main Text, in the Control Climate and the Uniformly Warmed Climate (Indicated by Numbers After the Arrow)

	Gray	SSM	RRTMG
Tropically averaged lapse-rate tropopause (hPa)	247 → 229	45 → 32	30 → 27
Tropically averaged radiative tropopause (hPa)	313 → 288	184 → 161	136 → 112
Eddy-driven jet latitude (°)	41.1 → 43.4	43.2 → 46.9	42.0 → 45.1
Subtropical jet latitude (°)	26.5 → 28.4	34.5 → 36.3	36.2 → 37.4
Hadley Cell width (°)	26.7 → 28.3	28.6 → 30.1	27.7 → 29.8
Hadley Cell strength (10^{10} kg s^{-1})	2.1 → 1.9	3.4 → 2.9	4.7 → 3.8

All three radiation schemes exhibit an amplification of temperature change with altitude in the tropics (Figures 5a–5c), consistent with the expectation from moist adiabatic physics. However, the magnitude and vertical structure of tropical upper-tropospheric amplification differs substantially between the gray model and RRTMG/SSM. To quantify this, we calculate an "amplification factor" as the ratio of tropically averaged (±30°N with area weighting) temperature change at 200 hPa compared to the change at 1,000 hPa. The amplification factor is 1.68 for gray radiation, compared to 2.37 for SSM and 2.35 for RRTMG. Visually, it is also apparent that the gray model produces weaker warming of the subtropical troposphere compared to RRTMG or SSM.

Under warming we also expect the tropopause to move to higher altitudes (McKim et al., 2025; Santer et al., 2003; Vallis et al., 2015), and this expectation is borne out in all three radiation schemes. Quantitatively, the pressure of the tropically averaged radiative tropopause changes from 313 hPa to 288 hPa for gray, 184 hPa to 161 hPa for SSM, and 134 hPa to 108 hPa for RRTMG. The magnitude of the vertical shift is similar between all schemes, and consistent with the simple scaling of about 6 hPa K^{-1} proposed by Match and Fueglistaler (2021).

All schemes exhibit a poleward shift of the subtropical and eddy-driven jet by $\approx 1-2$ degrees (Figures 5d–5f). The poleward shift of the eddy-driven jet is visually evidenced by the contrasting zonal-wind changes on either side of the surface westerlies. All schemes also simulate an intensification of the surface easterlies on the equator, and a general weakening of westerlies on the equatorward side of the jet. However, the gray model produces changes in the upper-troposphere which differ from RRTMG or SSM. Most notably, while all schemes produce a super-rotating equatorial jet in their control climates which shifts upwards with warming, the gray model is the only configuration which features a strong intensification of the super-rotation with warming. Additionally, while RRTMG and SSM produce a weakening of the upper-tropospheric flow on the equatorward side of the jet, the gray model produces a strengthening on the equatorward side of the upper-tropospheric jet core. This is possibly related to an intensification of the subtropical jet, which is still "split" from the eddy-driven jet in the gray model in response to uniform warming.

These gray radiation results, in which the subtropical and eddy-driven jets shift poleward with warming, appear contrary to previous work which has reported that the jet shifted *equatorward* with warming in gray radiation models (Dwyer & O'Gorman, 2017; Lachmy & Shaw, 2018; Schneider et al., 2010; Tan et al., 2019). However, previous studies which have found an equatorward shift have used slab ocean simulations (with no Q-flux) and then directly perturbed the longwave optical depth to simulate climate change, whereas we use a prescribed SST profile which is then uniformly warmed. It appears that the equatorward jet shift seen in previous studies is sensitive to this methodological choice. We find that if we repeat our experiments but use the experimental design of these previous studies, we can reproduce the equatorward shift of the eddy-driven jet and surface westerlies (Figure S2 in Supporting Information S1).

All three scheme yield a weakening and poleward expansion of the Hadley Cell (Table 2). The Hadley Cell width, diagnosed as the latitude closest to the equator where the streamfunction (vertically averaged with mass weighting between 700 and 300 hPa) is zero (Byrne et al., 2018), increases by $\approx 1-2$ degrees in all configurations. Similarly the Hadley Cell strength, diagnosed by vertically averaging the streamfunction magnitude with mass weighting between 700 and 300 hPa and then taking the meridional average between the equator and the cell edge, decreases in all schemes. However, changes in Hadley Cell strength are muted in the gray model compared to RRTMG or the SSM (Table 2). We also note that the vertical structure of Hadley Cell changes is different between the gray model and SSM/RRTMG. RRTMG and SSM have streamfunction changes which maximize in the upper-troposphere, whereas the gray model has streamfunction changes which maximize in the lower-troposphere, and in fact the gray model exhibits *increases* in the cell-mean Hadley Cell strength in the upper troposphere.

These GCM results show that our SSM is able to accurately represent the large-scale structure of the atmosphere and its response to climate change compared to RRTMG, which is validated in this range of temperatures and thus can be taken as a benchmark. This is in stark contrast to the gray model, which distorts many aspects of the large-scale atmospheric circulation and its response to warming. These conclusions are not sensitive to the precise formulation of the gray scheme (Appendix C), and also hold when using slab ocean simulations in place of fixed-SST forcing (Appendix B). This demonstrates that a simplified representation of H_2O and CO_2 spectroscopy is sufficient to capture the key features of radiation-dynamics coupling in both current and future Earth-like climates.

4. What New Science Does the SSM Enable?

What science questions can be answered with the SSM that might prohibitively difficult to tackle with more comprehensive correlated-k schemes? In this section we will briefly note some of the new insights and avenues for investigation which the SSM makes accessible.

To start with, the SSM can output relatively detailed, spectrally resolved fields such as outgoing longwave radiation (OLR). This is in contrast to RRTMG or other correlated-k models, which only output broadband fluxes or coarse, band-averaged, fluxes. The SSM's new level of spectral detail allows one to gain new physical insights into the behavior of the climate system.

To illustrate the utility of this spectrally resolved output we will briefly examine the spectrally resolved climate feedback parameter (defined as the extra longwave radiation emitted to space per degree of global warming) in the SSM simulations. Understanding the climate feedback parameter is critical for constraining equilibrium climate sensitivity (e.g., Sherwood et al., 2020), and previous work has demonstrated the utility of viewing the feedback parameter through a spectral lens (e.g., Huang et al., 2014; Koll et al., 2023; Pan & Huang, 2018; Seeley & Jeevanjee, 2021). However, previous work has mostly focused on single-column models because running line-by-line radiation schemes on full GCM fields is prohibitively expensive.

The SSM allows one to take a spectrally resolved perspective on the feedback parameter in GCM simulations, as shown in Figure 6. Figure 6a shows the spectrally- and latitudinally resolved climate feedback parameter in response to uniform +4 K warming, and Figure 6c shows the spectrally resolved, global-mean feedback parameter. The spectral- and latitudinal-structure of the feedback parameter has a number of interesting features, and we will touch on a few of these now.

The first thing to note is that the feedback parameter is dominated by the water vapor "window" region, centered around $\approx 1000\ \mathrm{cm}^{-1}$, where H_2O is optically thin and the surface can emit directly to space (further discussion in Appendix A). However, not all latitudes exhibit this behavior. Notably, the feedback parameter in the tropical window region (equatorward of 20°) is quite weak. This is because in response to +4 K warming, the window starts to become optically thick due to H_2O continuum absorption. This masks the enhanced surface emission which would otherwise be emitted to space, weakening the feedback parameter.

Another striking feature of Figure 6a is the enhanced longwave emission to space from the edges of the CO_2 band near $660\ \mathrm{cm}^{-1}$; previous work has termed this feature the "CO_2 radiator fin" (Seeley & Jeevanjee, 2021). Because CO_2 is well-mixed, its emission levels (where $\tau_{\tilde{\nu}} = 1$) are fixed functions of pressure. Warming of the troposphere thus enhances OLR to space by warming the CO_2 emission levels. The center of the CO_2 band hits $\tau_{\tilde{\nu}} = 1$ in the stratosphere, hence the lack of a stronger feedback in this region in response to tropospheric warming. The feedback from the edges of the CO_2 band is stronger in the tropics than in the extratropics, because CO_2 has emission levels in the upper troposphere which experienced enhanced warming associated with moist adiabatic amplification of temperature changes in the tropical upper-troposphere (Figure 5b). These tropical upper-tropospheric emission levels warm more than the +4 K surface warming and thus have a stronger feedback.

Two final noteworthy features of Figure 6a are the "broadening" of the H_2O window at around 30° latitude (near $500\ \mathrm{cm}^{-1}$ and $1300\ \mathrm{cm}^{-1}$), and the subtle weakening of the feedback parameter at around 10° latitude in the H_2O bands (between 0 and $500\ \mathrm{cm}^{-1}$ and 1300–$2000\ \mathrm{cm}^{-1}$). We can explain this by reference to Figure 6b, which

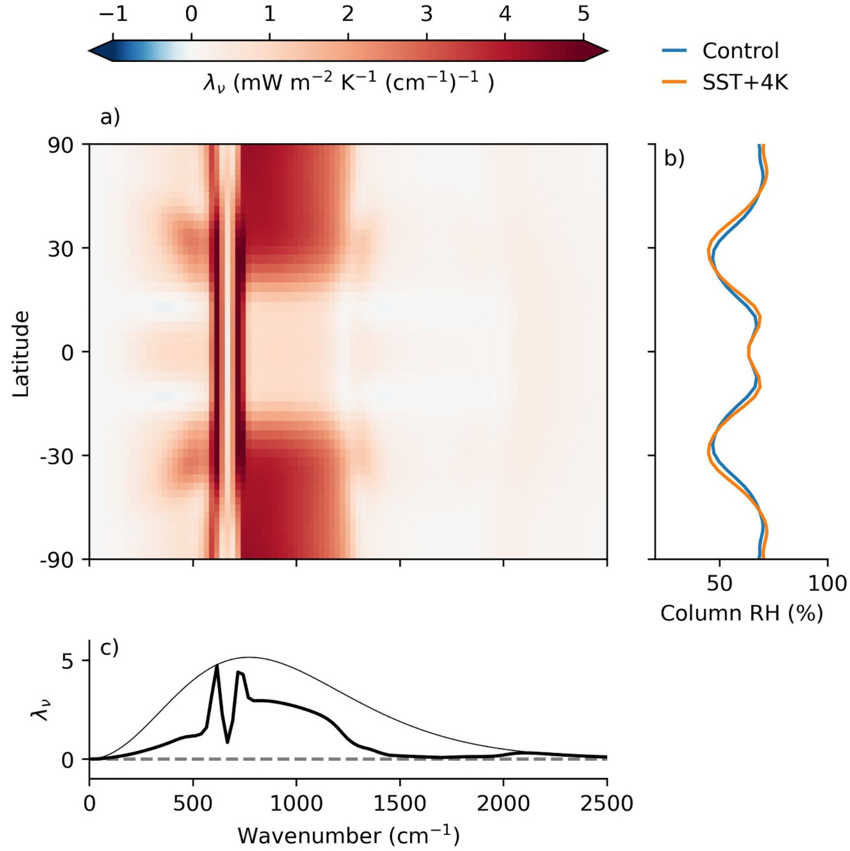

Figure 6. (a) The SSM feedback parameter as a function of latitude and wavenumber. (b) The column-averaged relative humidity (RH) as a function of latitude for the Control simulation and the uniform warming simulation. (c) The globally averaged, spectrally resolved feedback parameter from the SSM. Panels (a, b) share the same latitude axis, and panels (a, c) share the same wavenumber axis.

shows the column-averaged relative humidity (RH) as a function of latitude for the control and +4 K runs. Under warming, the subtropical minima in RH move polewards, leading to an increase in RH on the equatorward side of the minima and a decrease in RH on the poleward side. These changes in RH with warming affect the temperatures at which H_2O emits to space, thus altering the spectral feedbacks. To see this, we can write the H_2O optical depth in temperature coordinates as (using Equation 3, hydrostatic balance, and the definition of the lapse-rate),

$$\tau_{\tilde{\nu}}(T) = \mathcal{D}\int_{T_{tp}}^{T} \kappa(\tilde{\nu}, p(T))\rho_v(T')\,\frac{dT'}{\Gamma(T')} \tag{12}$$

where T_{tp} is the tropopause temperature, κ is the absorption coefficient, $\rho_v = \frac{\mathrm{RH}\,e^*(T)}{R_v T}$ is the vapor density, and $\Gamma(T)$ is the lapse-rate at temperature T (Jeevanjee, Koll, & Lutsko, 2021). Increases in relative humidity increase the value of ρ_v for a given temperature, and thus means that we need to integrate *less* far down into the atmosphere before we hit $\tau_{\tilde{\nu}} = 1$. Hence, increases in RH yield a decrease in emission temperature at wavenumbers where H_2O is optically thick, weakening the feedback in that region. This argument also holds for decreases in RH, which lead to an increase in H_2O emission temperatures, amplifying the spectral feedback in this region. These arguments are confirmed using offline radiative transfer calculations in Figure S3 in Supporting Information S1.

Another benefit of the SSM is that its transparent and equation-based construction makes it simple to alter the scheme in service of creative, hypothesis-driven experiments. For example, previous work has shown that the H_2O continuum is important for determining characteristics of radiative cooling and precipitation in very warm climates (Cohen & Pincus, 2025; Liu et al., 2024; Seeley & Wordsworth, 2021), but our understanding of how continuum absorption shapes the global atmospheric circulation is still under-developed. Using the SSM, one could conduct simulations where the strength of continuum absorption is varied (Equation 6) to explore how this affects the current climate and its response to global warming. Similarly, we have only considered the primary CO_2 band in our SSM (Equation 5), but one could easily add the "secondary" CO_2 bands into the SSM and evaluate their impact on the atmospheric circulation. The SSM also makes it possible to answer more fundamental questions, such as: What role does pressure broadening have in determining climate sensitivity? Feng et al. (2023) hypothesized that pressure broadening helps to guard Earth against the runaway greenhouse limit, and it would be possible to systematically test this in GCM simulations with the SSM by not applying the pressure-broadening prefactors in Equations 7–9. Conducting such an experiment in a modern correlated-k code would be very difficult, but is straightforward in the SSM. Enabling this form of hypothesis-driven experimentation is a key strength of the SSM.

5. Conclusions

We began this paper by noting a conspicuous gap in the hierarchy of radiative transfer schemes used in climate modeling; there are accurate, but somewhat opaque, correlated-k schemes and conceptually simple, but inaccurate, gray schemes. To bridge this "clarity-accuracy" gap, we have introduced a new clear-sky, longwave radiative transfer scheme—the Simple Spectral Model (SSM). Previous work has shown that significant theoretical insight into radiative transfer problems can be gained by representing the spectral structure of absorption coefficients using piece-wise analytic fits (e.g., Fildier et al., 2023; Jeevanjee & Fueglistaler, 2020b; Koll et al., 2023; McKim et al., 2025). Our SSM leverages this insight to build a clear-sky, longwave radiative transfer scheme suitable for idealized climate models which is both easily intelligible and reasonably accurate.

When implemented in an idealized GCM, the SSM produces zonal-mean climates that are much closer to those of the benchmark correlated-k scheme RRTMG than to the widely used gray radiation scheme of Frierson et al. (2006). Notable improvements are found in the representation of radiative cooling profiles, tropopause structure, atmospheric jets, and the Hadley Cell both in the control climate and in the response to uniform warming.

Correlated-k schemes are usually based on pre-calibrated lookup tables and thus are susceptible to errors when pushed outside of their training data (e.g., Kluft et al., 2021; Popp et al., 2016). In contrast to this, the SSM is equation-based and thus maintains physical consistency across a wide range of climates (Appendix A). The SSM also provides detailed spectral output, in contrast to broadband schemes, which greatly aids physical interpretation of results.

Future work could extend the SSM framework to include shortwave absorption by water vapor, in a similar manner to Roemer et al. (2025). This would allow the SSM to reproduce the negative hydrological sensitivity in hothouse climates noted by Liu et al. (2024), and to better understand the role of shortwave absorption on the general circulation of the atmosphere (W. Kang & Wordsworth, 2019). The SSM framework could also be extended to include simple representations of scattering and clouds (Pierrehumbert, 2010). While we have focused on including spectral representations of H_2O and CO_2, this could easily be updated to include other species, allowing exploration of methane-rich climates such as Titan (Mitchell & Lora, 2016) or exoplanets with even more exotic atmospheres (Alderson et al., 2023; Kempton et al., 2011).

We have demonstrated that the SSM is a useful tool for idealized climate modeling and fills in an important gap in the "hierarchy" of radiative transfer models. We also envisage this SSM being useful in classroom settings by helping students form a clearer link between the textbook physics of radiative transfer and the simulation of radiative transfer in GCMs. More broadly, this work contributes to closing the long-standing gap between simulation and understanding in climate modeling (Held, 2005).

Appendix A: State-Dependence of Longwave Feedbacks in the SSM

To examine the behavior of the SSM (and the gray model, for comparison) across a wide range of climate states, we conducted single-column radiative-convective equilibrium simulations with Isca (McKim et al., 2025) over prescribed sea surface temperatures (SSTs) with a vertically constant relative humidity of 70%. Our focus here is on the state-dependence of longwave radiative feedbacks and how the schemes represent high-temperature regimes.

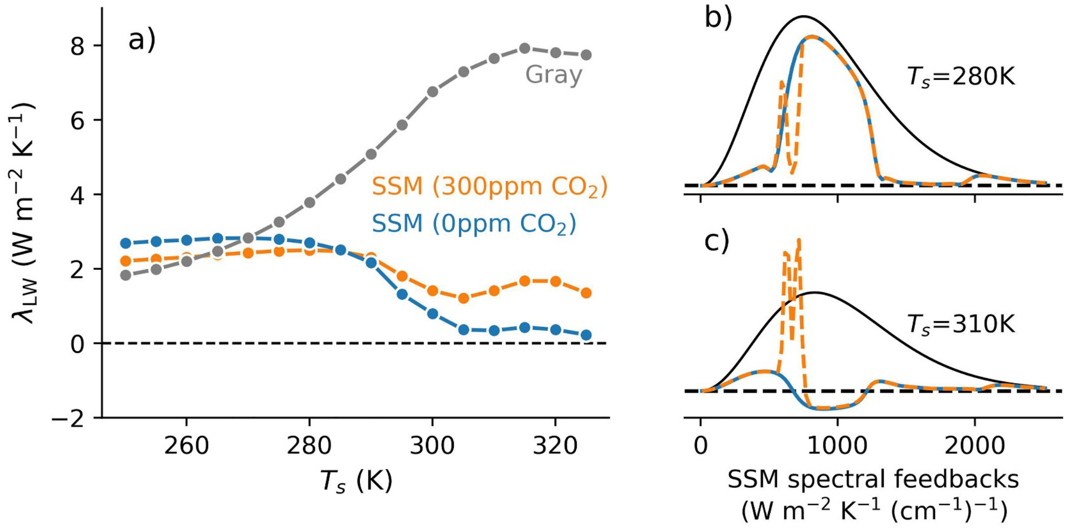

Figure A1. (a) State-dependence of the clear-sky longwave feedback parameter, λ_{LW}, in fixed-SST single-column runs using gray radiation, and the simple spectral model (SSM). The SSM simulations are conducted with 0 and 300 ppm of CO_2. Panels (b, c) show the spectrally resolved feedback parameter from the SSM for two baseline SSTs, blue solid curve is for 0 ppm CO_2 and the orange dashed curve is for 300 ppm CO_2. Black curves in (b, c) are the surface Planck feedback. All curves in (b, c) are normalized by the maximum value of the surface Planck feedback in that climate.

The single-column model simulations were run with 200 vertical levels to ensure a well-resolved tropopause and stratosphere even in extremely warm climates. We prescribed SSTs ranging from 260K to 330K in 5K increments and computed the clear-sky longwave feedback parameter, λ_{LW}, in each climate as the change in outgoing longwave radiation per unit surface temperature change. The SSM simulations were run both without CO_2, to isolate H_2O effects, and then with a constant 300 ppm of CO_2. The gray radiation scheme, by contrast, has no explicit representation of different absorbing species (Frierson et al., 2006).

Figure A1a shows the clear-sky longwave feedback parameter, λ_{LW}, as a function of baseline SST for the three sets of experiments. Both SSM set-ups have $\lambda_{\mathrm{LW}} \approx 2$ W m^{-2} K^{-1} for SSTs below 290K. This value of λ_{LW} arises because H_2O optical depths are an approximately fixed function of temperature and thus it is the optically thin "window" regions which dominate changes in OLR with warming (Jeevanjee, Koll, & Lutsko, 2021; Simpson, 1928). Figure A1b illustrates this by showing the spectrally resolved change in OLR per degree of warming (i.e., the spectrally resolved λ_{LW}) in the SSM simulations for the 280K climate state. The vast majority of the extra OLR per degree warming is contributed by the window region centered around 1000 cm^{-1}. The orange dashed curve in Figure A1b shows the effect of adding a constant 300ppm of CO_2, which weakens the feedback at low temperatures by taking a "bite" out of the window region.

In warmer climates the exponential increase in water vapor with warming, coupled with the temperature-induced strengthening of the continuum due to self-broadening, causes the window regions to become optically thick. When this happens, the longwave feedback in the window region rapidly weakens as shown by the SSM's spectral feedback parameter at 310K in Figure A1c. This "closing of the water vapor window" is associated with a weakening of the total longwave feedback parameter (Figure A1a), which is particularly pronounced in the absence of CO_2, in line with line-by-line calculations (e.g., Goldblatt et al., 2013; Koll & Cronin, 2018; Koll et al., 2023). We note that Figure A1c actually shows negative (destabilizing) feedbacks in the window region at 310K, which is because of the weakening of the moist lapse rate with warming which means that the temperature at which $\tau = 1$ decreases slightly with warming (Equation 12).

Even in the H_2O-only case we expect that λ_{LW} will remain small and positive in the post-runaway state due to the influence of foreign pressure broadening (Feng et al., 2023), an expectation borne out by the SSM in Figure A1a and the positive (stabilizing) feedbacks at wavenumbers below 700 cm^{-1} in Figure A1c. However, the presence of CO_2 also helps to prevent a runaway. Even preindustrial levels of CO_2 are sufficient to substantially strengthen λ_{LW} in warm climates compared to the 0 ppm case, somewhat offsetting the effects of the closing of the water vapor window. The reason for this can be seen in Figure A1c, which shows that the presence of CO_2 causes additional outgoing longwave radiation to space from those wavenumbers where CO_2 is optically thick (just the 15 μm band, in our SSM). This is because CO_2 is well-mixed, and thus its $\tau = 1$ levels are fixed functions of *pressure* rather than temperature (Seeley & Jeevanjee, 2021). Warming of the troposphere thus leads to stabilizing feedbacks from CO_2. This is particularly evident near the center of the CO_2 band, which hits its $\tau = 1$ level in the upper-troposphere and thus experiences greater warming per 1K increase in surface temperature due to moist adiabatic amplification of temperature changes in the upper-troposphere.

Moving now to the gray model, we see that the gray radiation scheme exhibits an approximately monotonic increase in λ_{LW} with warming, reaching ≈ 8 W m^{-2} K^{-1} at the warmest SSTs. This unphysical behavior stems from the scheme's inability to represent the spectral nature of atmospheric absorption and the existence of "window" regions. Although "windowed-gray" models exist (e.g., Geen et al., 2016; Weaver & Ramanathan, 1995), these models assume that a fixed fraction of the longwave spectrum is covered by the window region and would thus miss the behavior in Figure A1. One could imagine parameterizing this "window fraction" as a function of SST, but at that point the number of ad hoc parameters becomes unwieldy and the resulting climate states can be rather sensitive to these tunable parameters.

The SSM captures the state-dependence of λ_{LW} highlighted by previous studies (e.g., Koll et al., 2023). This includes the value of $\lambda_{\mathrm{LW}} \approx 2$ W m^{-2} K^{-1} at colder SSTs, the closing of the water vapor window at around 305K, and the CO_2-dependence of λ_{LW} at high SSTs. This demonstrates that the large-scale spectral structure captured by our piecewise fits (Figure 3) is sufficient to represent the essential physics of water vapor feedbacks, even in extreme climate states.

Appendix B: Slab Ocean Simulations With Increased Solar Constant

Here we present slab ocean simulations with the longwave radiation hierarchy presented in the main text. This section, again, demonstrates that the SSM does a better job of emulating the RRTMG scheme's response to climate change than the gray scheme.

When comparing simulations with a slab ocean model, there new sources of discrepancy which are not present in the main text (where we used fixed-SST experiments). First, the slab ocean simulations with gray radiation, SSM, and RRTMG may have different SST profiles in their control runs. Second, the latitudinal structure of the forcing may be different. For example, the gray model does not represent CO_2, and so we can not perturb the longwave absorber in an equivalent way between the gray and SSM or RRTMG schemes.

To mitigate against the first issue, I have used a Q-flux approach to force all the slab ocean simulations to initially resemble the QOBS SST distribution used in the main text, following A. I. Williams and Merlis (2025). The q-flux is climate-invariant and thus only affects the SSTs in the control climate. I have verified that the zonal-mean fields in these simulations are similar to those in the fixed-SST simulations with the prescribed QOBS SST profile. To mitigate against the second issue, and achieve a cleaner comparison between the gray, SSM, and RRTMG schemes, I have opted to perturb all schemes with a +100 Wm^{-2} increase in the solar constant. This corresponds to a 25 Wm^{-2} radiative forcing in the global-mean; large, but helpful from a signal-to-noise standpoint. Taken together, this approach allows the three schemes to have the same initial SST profile, and an identical climate forcing, but to still produce their own energetically closed climate states in response to forcing. The divergence in the response to climate change is thus unambiguously attributable to differences in longwave radiative transfer, in contrast to Tan et al. (2019).

We note that RRTMG may start to experience out-of-bounds errors in the tropics in response to this magnitude of forcing (Kluft et al., 2021), but for the level of accuracy we are aiming for it is still adequate to consider RRTMG as a benchmark.

The slab ocean simulations have the insolation, I, prescribed as a time-independent function of latitude, ϕ, that approximates a perpetual annual-mean,

$$I(\phi) = \frac{S_0}{4}\left[1 + \frac{\Delta_s}{4}\left(1 - 3\sin^2(\phi)\right)\right], \tag{B1}$$

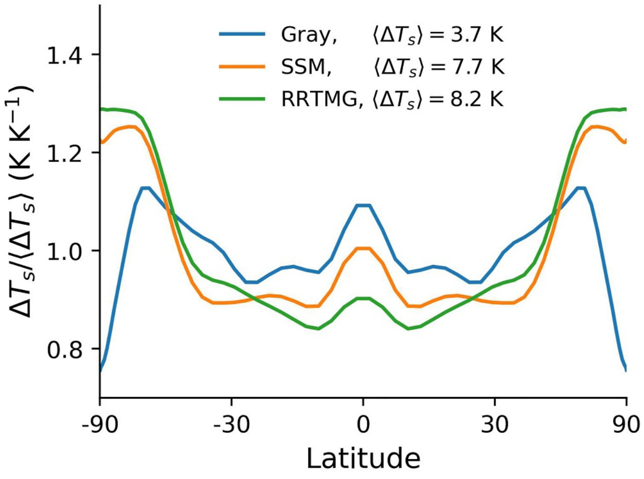

Figure B1. The change in zonal-mean surface temperature per degree of global-mean surface warming in the gray, SSM, and RRTMG runs. The change in global-mean sea-surface temperature ($\langle \Delta T_s \rangle$) for each run is shown in the legend.

where $S_0 = 1360$ Wm^{-2} in the control climate and $S_0 = 1460$ Wm^{-2} in the perturbed climate, and $\Delta_s = 1.4$ (following Frierson et al., 2006). As in the main text, there is no atmospheric absorption of solar radiation and thus the shortwave radiative heating rate is zero at all points in the atmosphere. There is no diurnal or seasonal cycle in the model. The surface albedo is equal to 0.22 and is globally uniform and climate-invariant.

The global-mean temperature change in the gray model is quite different from the SSM- or RRTMG-enabled models. In response to a 100 Wm^{-2} increase in the solar constant, the change in global-mean surface temperature is 3.7 K in the gray model, 7.7 K in the SSM model, and 8.2 K in the RRTMG model. The gray model thus underestimates the global-mean temperature change by more than a factor of 2, whereas the SSM closely emulates the RRTMG result.

In Figure B1 we show the zonal-mean surface temperature change, normalized by the global-mean surface temperature change, which highlights the pattern of warming in each run. The main difference between the simulations lies in the polar regions. The RRTMG model experiences moderate polar-amplified warming, which is similar in the SSM model, whereas the gray model has tropically amplified warming. To quantify this, we use the $\widetilde{\mathrm{PA}}$ metric from A. I. Williams and Merlis (2025), which measures the difference in temperature change between a polar cap and tropical average, normalized by the global-mean surface temperature:

$$\widetilde{\mathrm{PA}} \equiv \frac{\Delta T_s|_{\text{pole}}}{\langle \Delta T_s \rangle} - \frac{\Delta T_s|_{\text{trop}}}{\langle \Delta T_s \rangle}. \tag{B2}$$

The polar cap is bounded by 60° and the tropical average taken within 30° of the equator. We find that $\widetilde{\mathrm{PA}} \approx -0.08$ for the gray model, $\widetilde{\mathrm{PA}} \approx 0.32$ for the SSM model, and $\widetilde{\mathrm{PA}} \approx 0.41$ for the RRTMG model.

In Figure B2 we show the zonal-mean changes in temperature, zonal-wind and the mean meridional streamfunction, normalized by the change in global-mean surface temperature. As in the main text, we can see that the SSM does a better job of capturing the large-scale climate response of RRTMG than the gray model. The structure of temperature changes differ substantially between the gray model and RRTMG/SSM. For example, the ratio of tropical temperature change at 200 hPa to the tropical-mean temperature change at 1,000 hPa (the "amplification factor" defined in the main text) is 1.67 for the gray scheme, 2.41 for the SSM, and 2.36 for RRTMG. The gray scheme also exhibits much weaker warming of the polar free-troposphere compared to SSM/RRTMG, consistent with its lack of polar-amplified warming (Figure B1). All schemes exhibit a polewards shift of the eddy-driven jet (EDJ), but the gray scheme shifts the EDJ at a rate of $\approx 0.5°$ K^{-1}, whereas the SSM and RRTMG both shift the EDJ polewards at a rate of $\approx 0.1°$ K^{-1}. This stronger jet shift can be seen in the more pronounced dipole of zonal-mean zonal wind changes around the climatological EDJ latitude for the gray model (Figure B2d) versus SSM and RRTMG (Figures B2e and B2f).

The differences between SSM and RRTMG are slightly more pronounced in this slab ocean setup compared to the fixed-SST simulations in the main text. One of the main discrepancies is in the tropical upper troposphere, where the sign of the zonal-mean zonal wind response differs (panels e and f). This is likely linked to the stronger meridional temperature gradient which develops in the extratropical lower stratosphere in SSM (panel b), which drives an increase in zonal-mean zonal wind. However, especially when we take into account that the magnitude of the changes in the gray model are actually about half the size implied by the (normalized) changes in Figure B2, we can see that SSM much more accurately captures climate change as simulated by RRTMG.

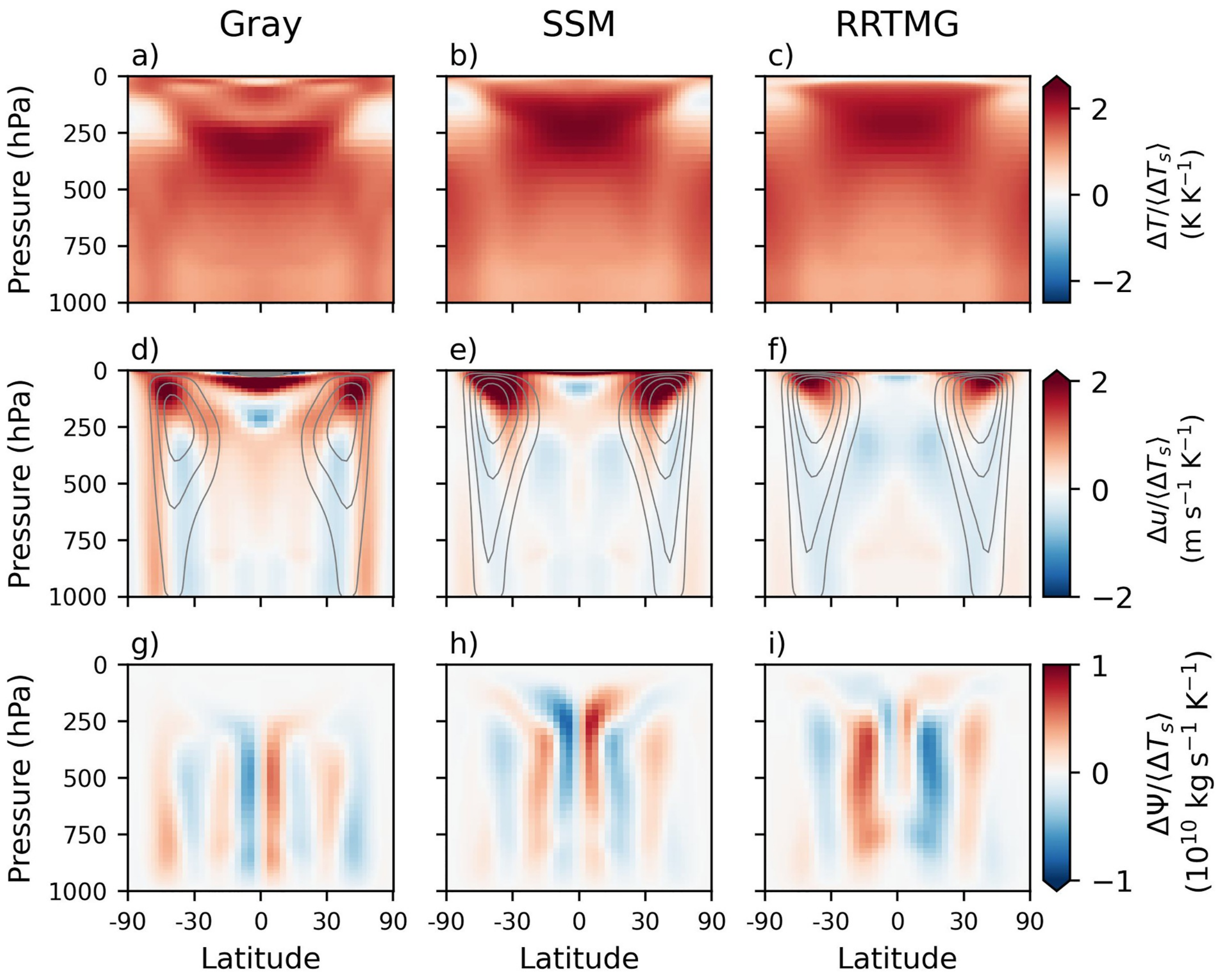

Figure B2. Zonal-mean changes in (a–c) temperature, (d–f) zonal wind, (g–i) mean meridional streamfunction in response to an increase in the solar constant. All fields are normalized by the change in global-mean surface temperature and thus the colorbars are different than in Figure 5. The contours in panels (g–i) have been removed to make it easier to see the streamfunction changes, but the climatological Hadley circulations look very similar to those in Figure 4.

Appendix C: Parameter-Dependence of the Gray Radiation Simulations

As noted in the main text, the gray scheme uses a prescribed longwave optical depth which is parameterized by Equation 10. This function has three free parameters, f, τ_e, and τ_p. In the main text, we use the parameter settings from Frierson et al. (2006) as this is the most common variant of the gray scheme. Subsequent studies have used alternative parameter settings, sometimes in an attempt to alleviate biases associated with gray radiation (e.g., Tan et al., 2019). In this appendix, we repeat the fixed-SST simulations conducted in the main text, but for three variants on the gray scheme which have been suggested in the literature. These variants are described in Table C1.

Table C1

Variations on the Parameter Settings in Equation 10, as Introduced by Different Papers in the Literature

	Frierson06	OGorman08	Tan19	Lewis24
f	0.1	0.2	0.2	0.2
τ_e	6	7.2	5.4	7.2
τ_p	1.5	1.8	3.13	3.6

Note. “Frierson06” is Frierson et al. (2006), “OGorman08” is O'Gorman and Schneider (2008), “Tan19” is Tan et al. (2019), “Lewis24” is Lewis et al. (2024).

Figure C1 shows that all four variants of the gray scheme exhibit similar large-scale biases in their zonal-mean radiative cooling, temperature, zonal wind, and mean meridional streamfunction. There are some differences, for instance the Frierson06 scheme has a warmer polar stratosphere and a weaker stratospheric jet compared to the other schemes, consistent with thermal wind balance. The degree to which the subtropical and eddy-driven jets are “split” also differs somewhat between the schemes. However, the main takeaway from this analysis is that the biases we identified in the main text are not strongly sensitive to the precise configuration of the gray radiation scheme we used.

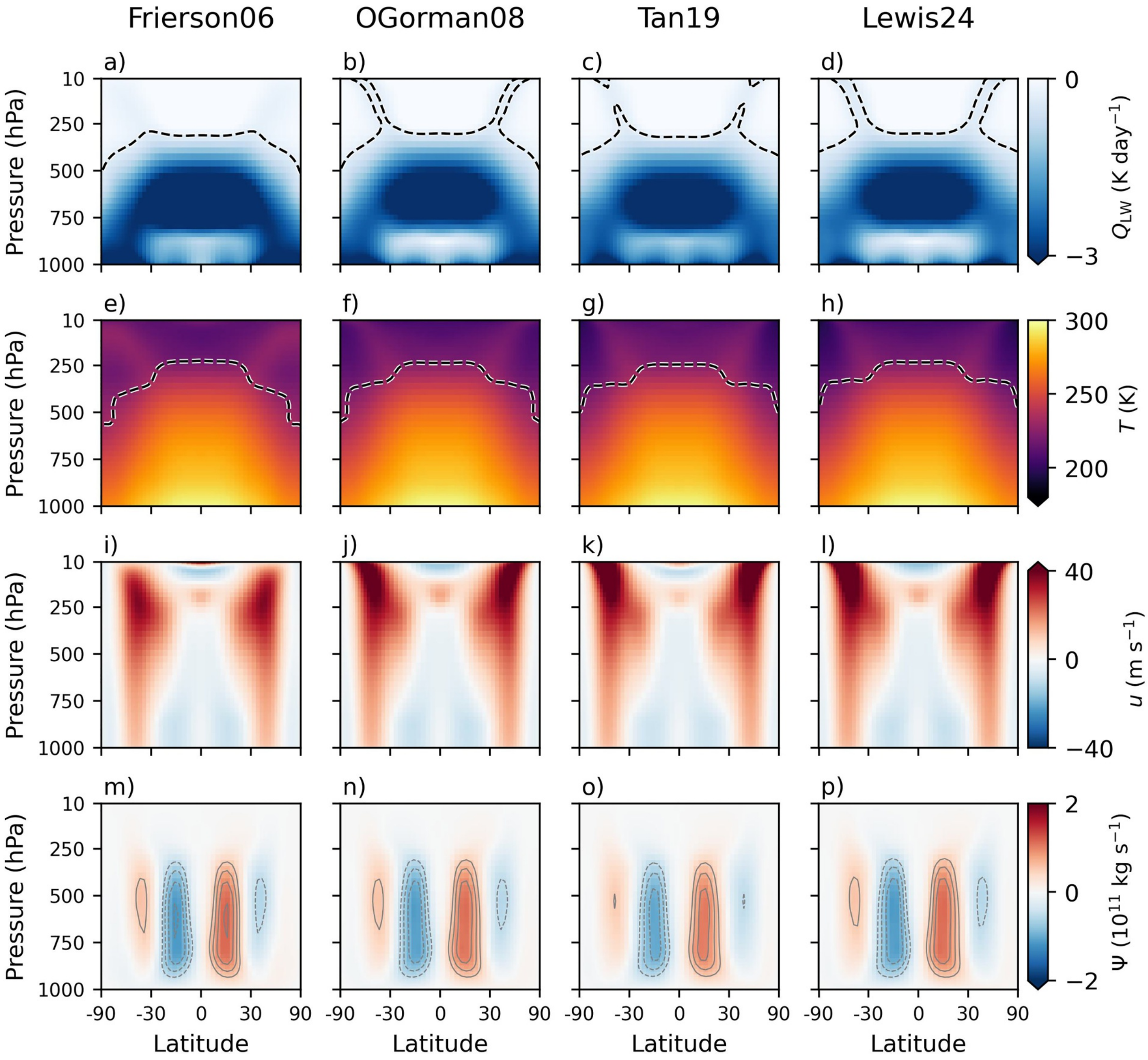

Figure C1. Zonal-mean (a–d) longwave radiative heating rate, (e–h) temperature, (i–l) zonal wind, and (m–p) mean meridional streamfunction for GCM simulations using different parameter settings for the gray radiation scheme. Each column refers to a different set of free parameters, outlined in Table C1. Contours are the same as Figure 4.

Figure C2 shows the response to uniform +4 K warming for all four variants of the gray scheme. As before, there are some quantitative differences between the response to warming in the different gray schemes. For example, the zonal-mean zonal wind response is larger in the Frierson06 scheme compared to the other three schemes, consistent with an increase in its meridional temperature gradient in the upper-troposphere and lower stratosphere. Note the Frierson06 scheme already underestimates the zonal wind changes compared to RRTMG and SSM in response to uniform +4 K warming. All schemes exhibit qualitatively similar jet shifts, tropospheric temperature changes, and Hadley Cell changes. Irrespective of the precise configuration of the gray scheme, we conclude that gray radiation still distorts the response of the atmospheric temperature and circulation to warming, in a way which is ameliorated when using the SSM radiation scheme.

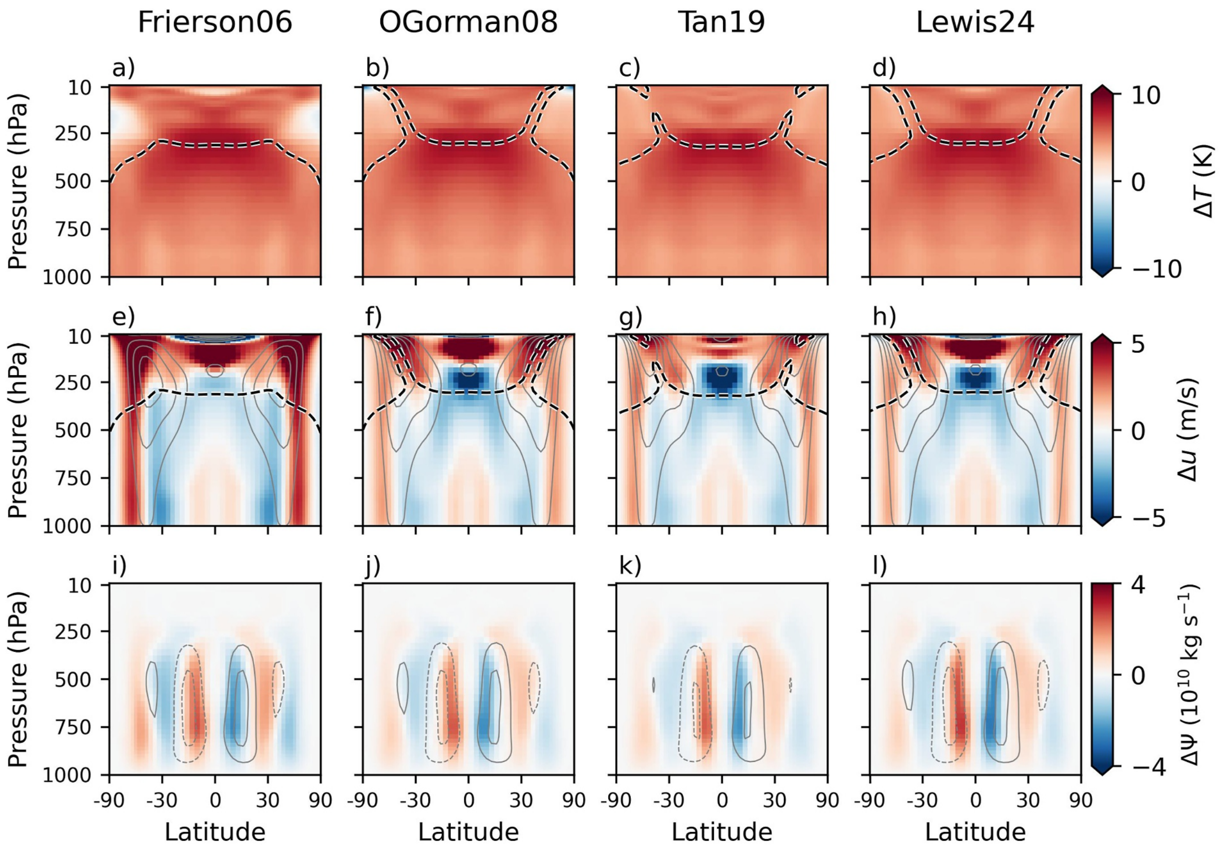

Figure C2. As in Figure C1, but showing the response to a uniform +4 K warming of the prescribed QOBS SST field. Note that the colorbars are different than in Figure 5 of the main text, so as to better highlight the relative differences between the gray schemes.

Conflict of Interest

The author declares no conflicts of interest relevant to this study.

Data Availability Statement

Data supporting the conclusions, and FORTRAN90 code to implement the SSM in Isca, are archived at A. I. L. Williams (2025).

Acknowledgments

A.I.L. Williams acknowledges funding from the CIMES Postdoctoral Fellowship under award NA18OAR4320123 from the National Oceanic and Atmospheric Administration, U.S. Department of Commerce. Thanks to Ilai Guendelman, Nadir Jeevanjee, Neil Lewis, Tim Merlis, and Robert Pincus for encouragement and helpful discussions; to Daniel Koll and two anonymous reviewers for their helpful feedback on the manuscript; and to Makayla and Cleo for moral and grammatical support.

References

Alderson, L., Wakeford, H. R., Alam, M. K., Batalha, N. E., Lothringer, J. D., Adams Redai, J., et al. (2023). Early release science of the exoplanet WASP-39b with JWST NIRSpec G395H. *Nature*, *614*(7949), 664–669. https://doi.org/10.1038/s41586-022-05591-3

Armstrong, B. (1968). Theory of the diffusivity factor for atmospheric radiation. *Journal of Quantitative Spectroscopy and Radiative Transfer*, *8*(9), 1577–1599. https://doi.org/10.1016/0022-4073(68)90052-6

Byrne, M. P., Pendergrass, A. G., Rapp, A. D., & Wodzicki, K. R. (2018). Response of the intertropical convergence zone to climate change: Location, width, and strength. *Current Climate Change Reports*, *4*, 355–370. https://doi.org/10.1007/s40641-018-0110-5

Clough, S. A., Iacono, M. J., & Moncet, J.-L. (1992). Line-by-line calculations of atmospheric fluxes and cooling rates: Application to water vapor. *Journal of Geophysical Research*, *97*(D14), 15761–15785. https://doi.org/10.1029/92jd01419

Cohen, S., & Pincus, R. (2025). A spectroscopic theory for how mean rainfall changes with surface temperature. *Science Advances*, *11*(19), eadv6191. https://doi.org/10.1126/sciadv.adv6191

Crisp, D., Fels, S. B., & Schwarzkopf, M. (1986). Approximate methods for finding CO_2 15-μm band transmission in planetary atmospheres. *Journal of Geophysical Research*, *91*(D11), 11851–11866. https://doi.org/10.1029/jd091id11p11851

Davis, N. A., & Birner, T. (2022). Eddy-mediated Hadley cell expansion due to axisymmetric angular momentum adjustment to greenhouse gas forcings. *Journal of the Atmospheric Sciences*, *79*(1), 141–159. https://doi.org/10.1175/jas-d-20-0149.1

Dwyer, J. G., & O'Gorman, P. A. (2017). Moist formulations of the Eliassen–Palm flux and their connection to the surface westerlies. *Journal of the Atmospheric Sciences*, *74*(2), 513–530.

Feng, J., Paynter, D., & Menzel, R. (2023). How a stable greenhouse effect on earth is maintained under global warming. *Journal of Geophysical Research: Atmospheres*, *128*(9), e2022JD038124. https://doi.org/10.1029/2022jd038124

Fildier, B., Muller, C., Pincus, R., & Fueglistaler, S. (2023). How moisture shapes low-level radiative cooling in subsidence regimes. *AGU Advances*, *4*(3), e2023AV000880. https://doi.org/10.1029/2023av000880

Frierson, D. M. W. (2007). The dynamics of idealized convection schemes and their effect on the zonally averaged tropical circulation. *Journal of the Atmospheric Sciences*, *64*(6), 1959–1976. https://doi.org/10.1175/jas3935.1

Frierson, D. M. W., Held, I. M., & Zurita-Gotor, P. (2006). A gray-radiation aquaplanet moist GCM. Part I: Static stability and eddy scale. *Journal of the Atmospheric Sciences*, *63*(10), 2548–2566. https://doi.org/10.1175/jas3753.1

Geen, R., Czaja, A., & Haigh, J. D. (2016). The effects of increasing humidity on heat transport by extratropical waves. *Geophysical Research Letters*, *43*(15), 8314–8321. https://doi.org/10.1002/2016gl070214

Goldblatt, C., Robinson, T. D., Zahnle, K. J., & Crisp, D. (2013). Low simulated radiation limit for runaway greenhouse climates. *Nature Geoscience*, *6*(8), 661–667. https://doi.org/10.1038/ngeo1892

Gordon, I. E., Rothman, L. S., Hill, C., Kochanov, R. V., Tan, Y., Bernath, P. F., et al. (2017). The HITRAN2016 molecular spectroscopic database. *Journal of Quantitative Spectroscopy and Radiative Transfer*, *203*, 3–69. https://doi.org/10.1016/j.jqsrt.2017.06.038

Guendelman, I., & Kaspi, Y. (2020). Atmospheric dynamics on terrestrial planets with eccentric orbits. *The Astrophysical Journal*, *901*(1), 46. https://doi.org/10.3847/1538-4357/abaef8

Held, I. M. (2005). The gap between simulation and understanding in climate modeling. *Bulletin America Meteorology Social*, *86*(11), 1609–1614. https://doi.org/10.1175/bams-86-11-1609

Hogan, R. J., & Matricardi, M. (2020). Evaluating and improving the treatment of gases in radiation schemes: The Correlated K-Distribution Model Intercomparison Project (CKDMIP). *Geoscientific Model Development*, *13*(12), 6501–6521. https://doi.org/10.5194/gmd-13-6501-2020

Huang, X., Chen, X., Soden, B. J., & Liu, X. (2014). The spectral dimension of longwave feedback in the CMIP3 and CMIP5 experiments. *Geophysical Research Letters*, *41*(22), 7830–7837. https://doi.org/10.1002/2014gl061938

Iacono, M. J., Delamere, J. S., Mlawer, E. J., Shephard, M. W., Clough, S. A., & Collins, W. D. (2008). Radiative forcing by long-lived greenhouse gases: Calculations with the AER radiative transfer models. *Journal of Geophysical Research*, *113*(D13), D13103. https://doi.org/10.1029/2008jd009944

Jeevanjee, N., & Fueglistaler, S. (2020a). On the cooling-to-space approximation. *Journal of the Atmospheric Sciences*, *77*(2), 465–478. https://doi.org/10.1175/jas-d-18-0352.1

Jeevanjee, N., & Fueglistaler, S. (2020b). Simple spectral models for atmospheric radiative cooling. *Journal of the Atmospheric Sciences*, *77*(2), 479–497. https://doi.org/10.1175/jas-d-18-0347.1

Jeevanjee, N., Hassanzadeh, P., Hill, S., & Sheshadri, A. (2017). A perspective on climate model hierarchies. *Journal of Advances in Modeling Earth Systems*, *9*(4), 1760–1771. https://doi.org/10.1002/2017ms001038

Jeevanjee, N., Koll, D. D., & Lutsko, N. (2021). "simpson's law" and the spectral cancellation of climate feedbacks. *Geophysical Research Letters*, *48*(14), e2021GL093699. https://doi.org/10.1029/2021gl093699

Jeevanjee, N., Seeley, J. T., Paynter, D., & Fueglistaler, S. (2021). An analytical model for spatially varying clear-sky CO_2 forcing. *Journal of Climate*, *34*(23), 9463–9480.

Kang, S. M., Held, I. M., Frierson, D. M. W., & Zhao, M. (2008). The response of the ITCZ to extratropical thermal forcing: Idealized slab-ocean experiments with a GCM. *Journal of Climate*, *21*(14), 3521–3532. https://doi.org/10.1175/2007jcli2146.1

Kang, S. M., & Polvani, L. M. (2011). The interannual relationship between the latitude of the eddy-driven jet and the edge of the Hadley cell. *Journal of Climate*, *24*(2), 563–568. https://doi.org/10.1175/2010jcli4077.1

Kang, W., & Wordsworth, R. (2019). Collapse of the general circulation in shortwave-absorbing atmospheres: An idealized model study. *The Astrophysical Journal Letters*, *885*(1), L18. https://doi.org/10.3847/2041-8213/ab4c43

Kaspi, Y., & Showman, A. P. (2015). Atmospheric dynamics of terrestrial exoplanets over a wide range of orbital and atmospheric parameters. *The Astrophysical Journal*, *804*(1), 60. https://doi.org/10.1088/0004-637x/804/1/60

Kempton, E. M.-R., Zahnle, K., & Fortney, J. J. (2011). The atmospheric chemistry of GJ 1214b: Photochemistry and clouds. *The Astrophysical Journal*, *745*(1), 3. https://doi.org/10.1088/0004-637x/745/1/3

Kluft, L., Dacie, S., Brath, M., Buehler, S. A., & Stevens, B. (2021). Temperature-dependence of the clear-sky feedback in radiative-convective equilibrium. *Geophysical Research Letters*, *48*(22), e2021GL094649. https://doi.org/10.1029/2021gl094649

Koll, D. D. B., & Cronin, T. W. (2018). Earth's outgoing longwave radiation linear due to H_2O greenhouse effect. *Proceedings of the National Academy of Sciences*, *115*(41), 10293–10298. https://doi.org/10.1073/pnas.1809868115

Koll, D. D. B., Jeevanjee, N., & Lutsko, N. J. (2023). An analytic model for the clear-sky longwave feedback. *Journal of the Atmospheric Sciences*, *80*(8), 1923–1951. https://doi.org/10.1175/jas-d-22-0178.1

Lachmy, O., & Shaw, T. (2018). Connecting the energy and momentum flux response to climate change using the Eliassen–Palm relation. *Journal of Climate*, *31*(18), 7401–7416. https://doi.org/10.1175/jcli-d-17-0792.1

Levine, X. J., & Schneider, T. (2011). Response of the Hadley circulation to climate change in an aquaplanet GCM coupled to a simple representation of ocean heat transport. *Journal of the Atmospheric Sciences*, *68*(4), 769–783. https://doi.org/10.1175/2010jas3553.1

Lewis, N. T., England, M. R., Screen, J. A., Geen, R., Mudhar, R., Seviour, W. J., & Thomson, S. I. (2024). Assessing the spurious impacts of ice-constraining methods on the climate response to sea ice loss using an idealized aquaplanet GCM. *Journal of Climate*, *37*(24), 6729–6750. https://doi.org/10.1175/jcli-d-24-0153.1

Liu, J., Yang, J., Ding, F., Chen, G., & Hu, Y. (2024). Hydrologic cycle weakening in hothouse climates. *Science Advances*, *10*(17), eado2515. https://doi.org/10.1126/sciadv.ado2515

Lutsko, N. J., & Popp, M. (2018). The influence of meridional gradients in insolation and longwave optical depth on the climate of a gray radiation GCM. *Journal of Climate*, *31*(19), 7803–7822. https://doi.org/10.1175/jcli-d-18-0103.1

Match, A., & Fueglistaler, S. (2021). Large internal variability dominates over global warming signal in observed lower stratospheric QBO amplitude. *Journal of Climate*, *34*(24), 9823–9836.

McKim, B. A., Jeevanjee, N., Vallis, G. K., & Lewis, N. T. (2025). Water vapor spectroscopy and thermodynamics constrain Earth's tropopause temperature. *AGU Advances*, *6*(2), e2024AV001206. https://doi.org/10.1029/2024av001206

Merlis, T. M., & Schneider, T. (2010). Atmospheric dynamics of Earth-like tidally locked aquaplanets. *Journal of Advances in Modeling Earth Systems*, *2*(4), 17. https://doi.org/10.3894/james.2010.2.13

Mitchell, J. L., & Lora, J. M. (2016). The climate of Titan. *Annual Review of Earth and Planetary Sciences*, *44*(1), 353–380. https://doi.org/10.1146/annurev-earth-060115-012428

Mlawer, E. J., Payne, V. H., Moncet, J.-L., Delamere, J. S., Alvarado, M. J., & Tobin, D. C. (2012). Development and recent evaluation of the MT_CKD model of continuum absorption. *Philosophical Transactions of the Royal Society A: Mathematical, Physical and Engineering Sciences*, *370*(1968), 2520–2556. https://doi.org/10.1098/rsta.2011.0295

Mlawer, E. J., Taubman, S. J., Brown, P. D., Iacono, M. J., & Clough, S. A. (1997). Radiative transfer for inhomogeneous atmospheres: RRTM, a validated correlated-k model for the longwave. *Journal of Geophysical Research*, *102*(D14), 16663–16682. https://doi.org/10.1029/97jd00237

Mlynczak, M. G., Daniels, T. S., Kratz, D. P., Feldman, D. R., Collins, W. D., Mlawer, E. J., et al. (2016). The spectroscopic foundation of radiative forcing of climate by carbon dioxide. *Geophysical Research Letters*, *43*(10), 5318–5325. https://doi.org/10.1002/2016gl068837

Neale, R. B., & Hoskins, B. J. (2000). A standard test for AGCMs including their physical parametrizations: I: The proposal. *Atmospheric Science Letters*, *1*(2), 101–107. https://doi.org/10.1006/asle.2000.0022

O'Gorman, P. A., & Schneider, T. (2008). The hydrological cycle over a wide range of climates simulated with an idealized GCM. *Journal of Climate*, *21*, 3815–3832.

Pan, F., & Huang, X. (2018). The spectral dimension of modeled relative humidity feedbacks in the CMIP5 experiments. *Journal of Climate*, *31*(24), 10021–10038. https://doi.org/10.1175/jcli-d-17-0491.1

Petty, G. W. (2006). *A first course in atmospheric radiation*. Sundog publishing.

Pierrehumbert, R. T. (2010). *Principles of planetary climate*. Cambridge University Press.

Pincus, R., Mlawer, E. J., & Delamere, J. S. (2019). Balancing accuracy, efficiency, and flexibility in radiation calculations for dynamical models. *Journal of Advances in Modeling Earth Systems*, *11*(10), 3074–3089. https://doi.org/10.1029/2019ms001621

Pincus, R., Mlawer, E. J., Oreopoulos, L., Ackerman, A. S., Baek, S., Brath, M., et al. (2015). Radiative flux and forcing parameterization error in aerosol-free clear skies. *Geophysical Research Letters*, *42*(13), 5485–5492. https://doi.org/10.1002/2015gl064291

Popp, M., Schmidt, H., & Marotzke, J. (2016). Transition to a moist greenhouse with CO_2 and solar forcing. *Nature Communications*, *7*(1), 10627. https://doi.org/10.1038/ncomms10627

Reed, K. A., Medeiros, B., Jablonowski, C., Simpson, I. R., Voigt, A., & Wing, A. A. (2025). Why idealized models are more important than ever in Earth system science. *AGU Advances*, *6*(4), e2025AV001716. https://doi.org/10.1029/2025av001716

Roemer, F. E., Buehler, S. A., & Menang, K. P. (2025). How to think about the clear-sky shortwave water vapor feedback. *npj Climate and Atmospheric Science*, *8*(1), 1–10. https://doi.org/10.1038/s41612-025-01144-3

Romps, D. M., Seeley, J. T., & Edman, J. P. (2022). Why the forcing from carbon dioxide scales as the logarithm of its concentration. *Journal of Climate*, *35*(13), 4027–4047. https://doi.org/10.1175/jcli-d-21-0275.1

Santer, B. D., Sausen, R., Wigley, T., Boyle, J. S., AchutaRao, K., Doutriaux, C., et al. (2003). Behavior of tropopause height and atmospheric temperature in models, reanalyses, and observations: Decadal changes. *Journal of Geophysical Research*, *108*(D1), ACL–1. https://doi.org/10.1029/2002jd002258

Schneider, T., & O'Gorman, P. A. (2008). Moist convection and the thermal stratification of the extratropical troposphere. *Journal of the Atmospheric Sciences*, *65*, 3571–3583.

Schneider, T., O'Gorman, P. A., & Levine, X. J. (2010). Water vapor and the dynamics of climate changes. *Reviews of Geophysics*, *48*(3), RG3001. https://doi.org/10.1029/2009rg000302

Seeley, J. T., & Jeevanjee, N. (2021). H2o windows and CO_2 radiator fins: A clear-sky explanation for the peak in equilibrium climate sensitivity. *Geophysical Research Letters*, *48*(4), e2020GL089609. https://doi.org/10.1029/2020gl089609

Seeley, J. T., & Wordsworth, R. D. (2021). Episodic deluges in simulated hothouse climates. *Nature*, *599*(7883), 74–79. https://doi.org/10.1038/s41586-021-03919-z

Sherwood, S. C., Webb, M. J., Annan, J. D., Armour, K. C., Forster, P. M., Hargreaves, J. C., et al. (2020). An assessment of Earth's climate sensitivity using multiple lines of evidence. *Reviews of Geophysics*, *58*(4), e2019RG000678. https://doi.org/10.1029/2019rg000678

Shine, K. P., Ptashnik, I. V., & Rädel, G. (2012). The water vapour continuum: Brief history and recent developments. *Surveys in Geophysics*, *33*(3), 535–555. https://doi.org/10.1007/s10712-011-9170-y

Simpson, G. C. (1928). Some studies in terrestrial radiation. *Memoirs of the Royal Meteorological Society*, *2*(16), 69–95.

Singh, M. S., & O'Gorman, P. A. (2012). Upward shift of the atmospheric general circulation under global warming: Theory and simulations. *Journal of Climate*, *25*, 8259–8276.

Spaulding-Astudillo, F. E., & Mitchell, J. L. (2025). Clear-sky convergence, water vapor spectroscopy, and the origin of tropical congestus clouds. *AGU Advances*, *6*(1), e2024AV001300. https://doi.org/10.1029/2024AV001300

Stevens, B., & Kluft, L. (2023). A colorful look at climate sensitivity. *Atmospheric Chemistry and Physics*, *23*(23), 14673–14689. https://doi.org/10.5194/acp-23-14673-2023

Tan, Z., Lachmy, O., & Shaw, T. A. (2019). The sensitivity of the jet stream response to climate change to radiative assumptions. *Journal of Advances in Modeling Earth Systems*, *11*(4), 934–956. https://doi.org/10.1029/2018ms001492

Vallis, G. K., Colyer, G., Geen, R., Gerber, E., Jucker, M., Maher, P., et al. (2018). Isca, v1.0: A framework for the global modelling of the atmospheres of earth and other planets at varying levels of complexity. *Geoscientific Model Development*, *11*(3), 843–859. https://doi.org/10.5194/gmd-11-843-2018

Vallis, G. K., Zurita-Gotor, P., Cairns, C., & Kidston, J. (2015). Response of the large-scale structure of the atmosphere to global warming. *Quarterly Journal of the Royal Meteorological Society*.

Virtanen, P., Gommers, R., Oliphant, T. E., Haberland, M., Reddy, T., Cournapeau, D., et al. (2020). Scipy 1.0: Fundamental algorithms for scientific computing in python. *Nature Methods*, *17*(3), 261–272. https://doi.org/10.1038/s41592-019-0686-2

Waugh, D. W., Grise, K. M., Seviour, W. J., Davis, S. M., Davis, N., Adam, O., et al. (2018). Revisiting the relationship among metrics of tropical expansion. *Journal of Climate*, *31*(18), 7565–7581. https://doi.org/10.1175/jcli-d-18-0108.1

Weaver, C., & Ramanathan, V. (1995). Deductions from a simple climate model: Factors governing surface temperature and atmospheric thermal structure. *Journal of Geophysical Research*, *100*(D6), 11585–11591. https://doi.org/10.1029/95jd00770

Williams, A. I., & Merlis, T. M. (2025). State-dependence of polar amplification in an idealized, ice-free GCM. *Authorea Preprints*.

Williams, A. I. L. (2025). Supporting data for "bridging clarity and accuracy: A simple spectral longwave radiation scheme for idealized climate modeling" [Dataset]. *Zenodo*. https://zenodo.org/records/16817101

Wills, R. C., Levine, X. J., & Schneider, T. (2017). Local energetic constraints on Walker circulation strength. *Journal of the Atmospheric Sciences*, *74*(6), 1907–1922. https://doi.org/10.1175/jas-d-16-0219.1

Wilson, D. J., & Gea-Banacloche, J. (2012). Simple model to estimate the contribution of atmospheric CO_2 to the Earth's greenhouse effect. *American Journal of Physics*, *80*(4), 306–315. https://doi.org/10.1119/1.3681188

Wordsworth, R., Seeley, J., & Shine, K. (2024). Fermi resonance and the quantum mechanical basis of global warming. *The Planetary Science Journal*, *5*(3), 67. https://doi.org/10.3847/psj/ad226d

Zurita-Gotor, P., & Held, I. M. (2024). Factors controlling superrotation in a terrestrial aquaplanet. *Journal of the Atmospheric Sciences*, *81*(11), 1901–1920. https://doi.org/10.1175/jas-d-24-0080.1

Zurita-Gotor, P., & Held, I. M. (2025). Strong superrotation at high CO_2 in an idealized terrestrial aquaplanet. *Journal of Climate*.